

# High-Resolution $^{17}\text{O}$ Solid-State NMR as a Unique Probe for Investigating Oxalate Binding Modes in Materials: The Case Study of Calcium Oxalate Biominerals

Ieva Goldberg,<sup>\*</sup> Ivan Hung, Vincent Sarou-Kanian, Christel Gervais,<sup>\*</sup> Zhehong Gan, Jessica Novák-Spačková, Thomas-Xavier Métro, César Leroy, Dorothee Berthomieu, Arie van der Lee, Christian Bonhomme, and Danielle Laurencin<sup>\*</sup>



Cite This: *Inorg. Chem.* 2024, 63, 10179–10193



Read Online

ACCESS |



Metrics & More

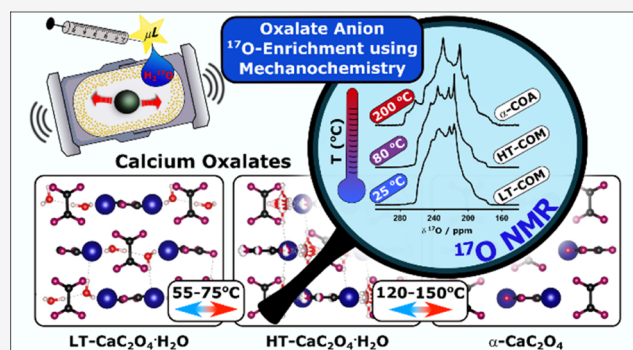


Article Recommendations



Supporting Information

**ABSTRACT:** Oxalate ligands are found in many classes of materials, including energy storage materials and biominerals. Determining their local environments at the atomic scale is thus paramount to establishing the structure and properties of numerous phases. Here, we show that high-resolution  $^{17}\text{O}$  solid-state NMR is a valuable asset for investigating the structure of crystalline oxalate systems. First, an efficient  $^{17}\text{O}$ -enrichment procedure of oxalate ligands is demonstrated using mechanochemistry. Then,  $^{17}\text{O}$ -enriched oxalates were used for the synthesis of the biologically relevant calcium oxalate monohydrate (COM) phase, enabling the analysis of its structure and heat-induced phase transitions by high-resolution  $^{17}\text{O}$  NMR. Studies of the low-temperature COM form (LT-COM), using magnetic fields from 9.4 to 35.2 T, as well as  $^{13}\text{C}$ – $^{17}\text{O}$  MQ/D-RINEPT and  $^{17}\text{O}\{^1\text{H}\}$  MQ/REDOR experiments, enabled the 8 inequivalent oxygen sites of the oxalates to be resolved, and tentatively assigned. The structural changes upon heat treatment of COM were also followed by high-resolution  $^{17}\text{O}$  NMR, providing new insight into the structures of the high-temperature form (HT-COM) and anhydrous calcium oxalate  $\alpha$ -phase ( $\alpha$ -COA), including the presence of structural disorder in the latter case. Overall, this work highlights the ease associated with  $^{17}\text{O}$ -enrichment of oxalate oxygens, and how it enables high-resolution solid-state NMR, for “NMR crystallography” investigations.



## INTRODUCTION

Oxalate anions are found in numerous molecules and materials across various disciplines, including geology, life science, and (nano)materials science. The small size and many different coordination modes of oxalate ligands toward metal centers explain the wide diversity of metal oxalate structures. Numerous studies have been carried out on transition metal oxalates, showing that they can be attractive as energy storage materials for  $\text{CO}_2$  capture, or as interesting components for Li-ion, Na-ion, and other redox batteries.<sup>1</sup> Furthermore, synthetic coordination networks containing oxalate anions have been widely investigated,<sup>2,3</sup> with luminescent properties in the case of lanthanum-based metal–organic frameworks (MOFs),<sup>4</sup> and magnetic properties for transition metal and lanthanide oxalates.<sup>5–7</sup> In the nuclear industry, oxalate ions are also used as a precipitating agent for purification and isolation purposes of actinides, which are further decomposed to obtain the corresponding oxides.<sup>8</sup> In Nature, there are over 20 minerals reported to contain oxalate ions,<sup>9</sup> chelating various cations found in soil and plants such as alkaline earth metals, transition metals, and rare earth elements.<sup>10–12</sup>

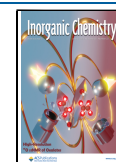
Calcium oxalate minerals are associated with pathological biomineralization processes in humans, leading to kidney stone disease (urolithiasis).<sup>13–15</sup> Notably, the monohydrate form ( $\text{CaC}_2\text{O}_4 \cdot \text{H}_2\text{O}$ , whewellite, COM) is the predominant phase in kidney stones.<sup>15,16</sup> Depending upon the temperature, whewellite can adopt two structures, so-called low- and high-temperature forms (denoted as LT and HT, respectively) (Figure 1). Upon further heat treatment (up to  $\sim 410^\circ\text{C}$ ), several anhydrous polymorphs can also be obtained synthetically ( $\text{CaC}_2\text{O}_4$ , noted COA),<sup>17,18</sup> which are unstable under ambient laboratory conditions and rehydrate back to the COM.<sup>18,19</sup> The transitions between these phases lead to changes in lattice cell parameters and local environments of the oxalates (Figures S1 and S2), with notably increased dynamics

Received: January 23, 2024

Revised: March 20, 2024

Accepted: April 2, 2024

Published: May 10, 2024



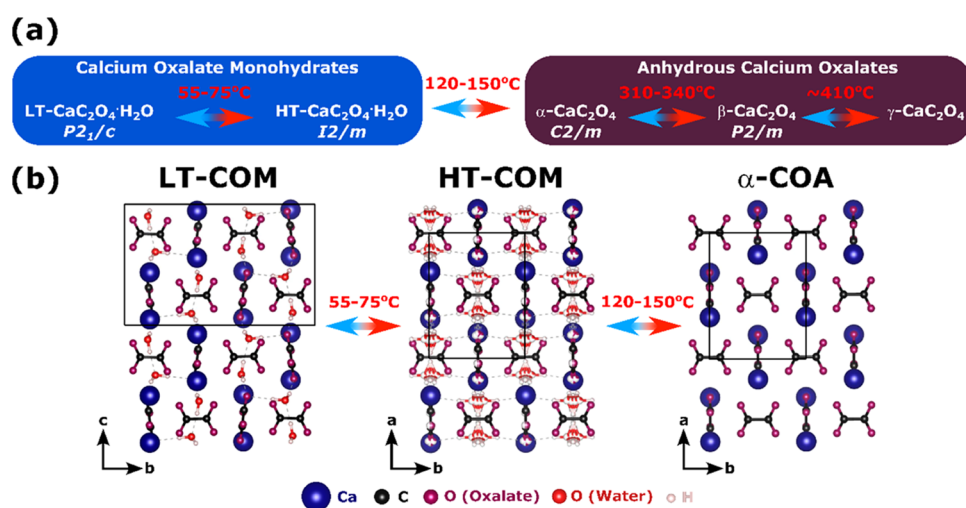


**Figure 1.** (a) Chemical and structural evolution of calcium oxalates upon heat treatment (as proposed by Izatulina et al.).<sup>17</sup> (b) Structural relationships between LT-COM, HT-COM, and α-COA. Note that the reported *I2/m* symmetry for HT-COM is equivalent to *C2/m* symmetry by a cell transformation and that the dehydration from HT-COM to α-COA is an isostructural process.

around the neighboring water molecules in the HT-COM, and variations in the distances to neighboring calcium cations.<sup>17,20</sup>

Due to the prevalence of oxalate anions in a wide variety of natural and synthetic structures, detailed studies of their local environment within materials like those mentioned above are essential. A precise description of their coordination modes can give insights into their chemical and physical properties. Such structural studies can be carried out using a wide range of analytical techniques, like infrared (IR) and Raman spectroscopies, solid-state nuclear magnetic resonance (ssNMR), and X-ray diffraction (XRD) (for crystalline phases). Despite their usefulness, each of these techniques has its shortcomings. IR and Raman studies can give information on the coordination of oxalate ions,<sup>21–23</sup> but cannot always differentiate between different polymorphs.<sup>24</sup> Powder and single-crystal XRD analysis can provide more structural information,<sup>4,25</sup> including polymorphism,<sup>17</sup> but is unsuitable for studying amorphous materials. Regarding ssNMR, studies on oxalate-containing materials have been carried out at natural abundance on the <sup>13</sup>C nucleus,<sup>26,27</sup> but have required isotopic enrichment for <sup>17</sup>O, due to its much lower natural abundance (~0.037% for <sup>17</sup>O, vs ~1.1% for <sup>13</sup>C).<sup>28,29</sup> As oxygen is directly involved in the binding to the metal centers, <sup>17</sup>O ssNMR is a promising probe for structural studies, especially when considering that the chemical shift range for carboxylate oxygens spans over 50 ppm (from ~250 to 300 ppm).<sup>30–32</sup> Furthermore, density functional theory (DFT) calculations have shown that the isotropic chemical shift ( $\delta_{\text{iso}}$ ) of oxalate oxygens is sensitive to the bonding strength of oxalate ion to the metal center.<sup>31</sup> However, in addition to poor sensitivity, <sup>17</sup>O ssNMR also suffers from poor spectral resolution due to the quadrupolar nature of the oxygen-17 (spin-5/2) nuclide, and isotopic enrichment is thus essential to carry out high-resolution analyses.

For calcium oxalates, the transformations between the different forms presented in Figure 1 have been investigated so far by XRD,<sup>17,18,33</sup> IR, and Raman spectroscopies,<sup>24,34</sup> as well as thermogravimetric analysis (TGA), scanning electron microscopy (SEM), or differential scanning calorimetry (DSC) techniques.<sup>33,35</sup> Moreover, multinuclear ssNMR analyses have been carried out, showing that the changes in the oxalate local

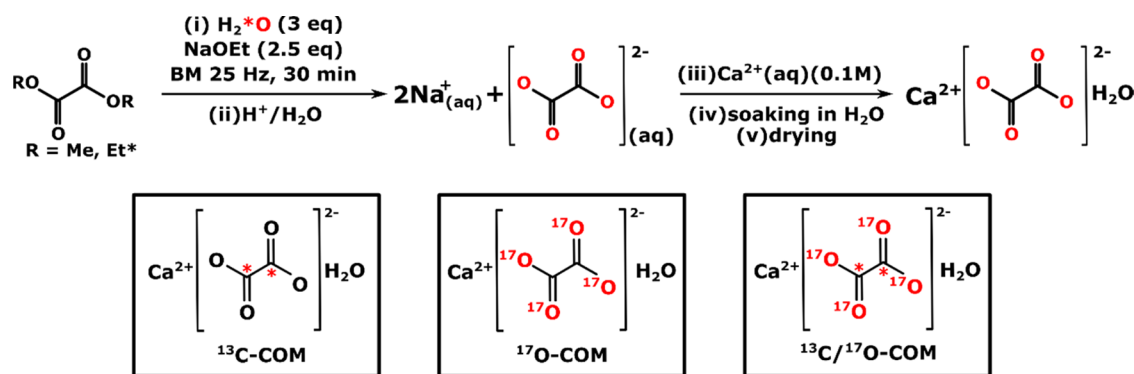
environment upon reversible transition of COM from the LT to the HT form can be followed by <sup>13</sup>C NMR,<sup>26</sup> and that the variations in dynamics of the water molecules during the same transformation can be investigated using <sup>17</sup>O and <sup>2</sup>H ssNMR (after isotopic enrichment of water with <sup>17</sup>O or <sup>2</sup>H).<sup>36</sup> Yet, to the best of our knowledge, no method has been proposed to probe directly the binding of the oxalate ligand oxygen atoms to its neighbors (i.e., calcium ions through coordination bonds, and protons of water molecules through hydrogen bonding). While <sup>17</sup>O ssNMR naturally appears as a promising method for studying oxalate oxygens, the enrichment procedures currently described in the literature (isotopic exchange starting from oxalic acid or sodium oxalate) involve up to 1 mL of <sup>17</sup>O-enriched water,<sup>28,29,37</sup> which can be particularly expensive and not optimal for subsequent syntheses of oxalate-based (nano)materials, considering the high cost of <sup>17</sup>O-labeled water (1800–2900 EUR for 1 mL of 90% oxygen-17 enriched H<sub>2</sub>O, as of publication date). Based on our recent developments of <sup>17</sup>O-labeling protocols for carboxylic groups using mechanochemistry, which enabled the efficient labeling of fatty acids and amino acids using only microliter quantities of H<sub>2</sub><sup>17</sup>O,<sup>38–40</sup> we decided (i) to test this enrichment methodology to the label oxalate oxygen atoms, and (ii) to demonstrate how such labeled ligands can then be used to probe via advanced <sup>17</sup>O ssNMR analyses the structure and reactivity of biominerals involved in pathological calcifications.

This article describes high-resolution <sup>13</sup>C and <sup>17</sup>O ssNMR studies of the LT-COM, HT-COM, and COA forms, including *in situ* variable-temperature investigations to monitor the changes occurring upon heat treatment. It will be shown that <sup>17</sup>O ssNMR analyses of oxalate binding provide highly complementary information compared to <sup>13</sup>C ssNMR, and can lead to valuable insights into the different phase transformations, further emphasizing that this technique can be valuable for the study of other oxalate systems.

## EXPERIMENTAL SECTION

**Reagents.** Dimethyl oxalate (C<sub>4</sub>H<sub>6</sub>O<sub>4</sub>, 99%, Alfa Aesar), diethyl oxalate (C<sub>6</sub>H<sub>10</sub>O<sub>4</sub>, 99%, Sigma-Aldrich), diethyl oxalate-<sup>13</sup>C<sub>2</sub> ((C<sub>2</sub>H<sub>5</sub>O<sub>2</sub><sup>13</sup>C)<sub>2</sub>, 99 atom % <sup>13</sup>C, Sigma-Aldrich), calcium chloride dihydrate (CaCl<sub>2</sub>·2H<sub>2</sub>O, 99%, Sigma-Aldrich), H<sub>2</sub><sup>17</sup>O (~40 or ~90% <sup>17</sup>O enrichment, CortecNet), H<sub>2</sub><sup>18</sup>O (99.3% <sup>18</sup>O enrichment,

**Scheme 1. Top: Synthetic Procedure of Isotopic Enrichment of Oxalate in COM Phase; Et\* Used Here to Designate the  $^{13}\text{C}$ -Labeled Diethyl Oxalate Precursor Enriched on the Carbonyl ( $\text{C}_2\text{H}_5\text{O}_2^{13}\text{C}$ ), Which Was Used for Preparing  $^{13}\text{C}$ - and  $^{13}\text{C}/^{17}\text{O}$ -COM<sup>a</sup>**



<sup>a</sup>Bottom: Chemical structures of the samples prepared for this study and their abbreviations used in the text. In the saponification reaction, based on the mechanism of this reaction, only one oxygen per function gets isotopically enriched; however, the label is distributed between both oxygen sites, due to the resonance of the carboxylate group, and as evident from  $^{17}\text{O}$  ssNMR analysis.

CortecNet), and sodium ethoxide (NaOEt, >95%, Sigma-Aldrich) were used as received. High-performance liquid chromatography (HPLC)-grade water (Acros Organics) was used for workup procedures and precipitation of COM.

**Synthesis of Isotopically Labeled COM: Isotopic Enrichment of Oxalates.** Preparation of  $^{17}\text{O}$ -COM (and  $^{18}\text{O}$ -COM). The enrichment of oxalate oxygens was achieved through mechanochemical saponification of an ester derivative of oxalic acid (Scheme 1), by adapting experimental procedures previously reported to prepare  $^{17}\text{O}/^{18}\text{O}$ -enriched fatty acids and amino acids.<sup>38,40</sup> The labeled hydroxy ions ( $\text{H}^*\text{O}^-$ ) are produced *in situ* by reaction of EtONa with  $\text{H}_2^*\text{O}$ , and react with the ester derivative of the carboxylic acid. Ball-milling (BM) experiments were performed on a Retsch Mixer Mill MM400 apparatus, using milling jars and beads predried under vacuum before the syntheses.

In a typical experiment, two stainless-steel beads (10 mm diameter) and a stainless-steel jar (inner volume 10 mL; screw-cap lid) were used. In the reactor, beads were introduced first, followed by dimethyl oxalate (134 mg, 1.13 mmol, 1.0 equiv), sodium ethoxide (190 mg, 2.80 mmol, 2.5 equiv), and isotopically enriched water (60.5  $\mu\text{L}$ , 3.36 mmol, 3 equiv). The reactor was closed and sealed using parafilm, and reagents were subjected to grinding for 30 min at 25 Hz. Attenuated total reflectance (ATR)-IR analyses confirmed the completion of the saponification by the shift in the carbonyl stretching vibration band from  $\sim 1735$  to  $\sim 1623$   $\text{cm}^{-1}$  (Figure S3). Then, HPLC grade water (1 mL) was added to the pasty, light beige reaction mixture. The jar was closed, sealed with parafilm, and further milled for 2 min at 25 Hz. The light beige solution was recovered and transferred to a conical flask. To ensure all product was retrieved, the milling jar was further washed with 4 mL of HPLC grade water and added to the conical flask. The pH of the solution was then adjusted to 6.5–7.0 using 1 M HCl ( $\sim 250$   $\mu\text{L}$ ).

The volume of the solution (containing solvated  $\text{Na}_2\text{C}_2^*\text{O}_4$ ) was then adjusted to reach a  $\sim 0.1$  M concentration for the oxalate. Separately, a  $\sim 0.1$  M aqueous solution of  $\text{CaCl}_2$  was prepared. Both solutions (of equimolar concentrations) were then introduced in separate syringes (with a typical volume of  $\sim 11.1$  mL), and added simultaneously with a syringe pump at a rate of 0.25 mL/min in a round-bottom flask, initially containing 1 mL of HPLC grade water, under magnetic stirring. The formation of a white precipitate was observed instantaneously. The reaction mixture was left under magnetic stirring for approximately 1 h. The white solid was filtered and dried under vacuum at room temperature ( $\sim 18$  h).

The final product ( $149 \pm 2$  mg) was found to be a mixture of calcium oxalate monohydrate (COM) and dihydrate (COD) phases, as shown by powder XRD (pXRD) and ATR-IR analyses (see Figures S4a and S5a). To obtain phase pure COM, the white solid was soaked

in  $\sim 1.5$  mL of HPLC grade water in a 2 mL Eppendorf tube and left immersed for 72 h at room temperature (without stirring). Excess water was removed by centrifugation at 20,000 rpm for 10 min, and the remaining solid was then dried under vacuum for 6 h. In cases when traces of COD were still observed (by pXRD and ATR-IR analysis), the solid was subjected to further soaking in water and drying cycles until no dihydrate was detected by these two analytical techniques.

**Preparation of  $^{13}\text{C}$ -COM and  $^{13}\text{C}/^{17}\text{O}$ -COM.** The  $^{13}\text{C}$ -enriched COM phase ( $^{13}\text{C}$ -COM) was prepared following a procedure analogous to the one described in the previous section. However, instead of dimethyl oxalate, diethyl oxalate- $^{13}\text{C}_2$  ( $150 \pm 1$   $\mu\text{L}$ , 1.0 equiv) was used as a precursor to yield  $^{13}\text{C}$  enrichment in oxalate carbon atoms, and HPLC grade water was used instead of enriched water in the saponification step. The fact that diethyl oxalate is a liquid in ambient laboratory conditions (while dimethyl oxalate is a solid) did not change the outcome of the reaction.

A doubly enriched COM phase ( $^{13}\text{C}/^{17}\text{O}$ -COM) was also prepared using diethyl oxalate- $^{13}\text{C}_2$  and  $\text{H}_2^{17}\text{O}$  ( $\sim 90\%$   $^{17}\text{O}$ ).

For these syntheses, the white precipitate (typically obtained in quantities  $\sim 155 \pm 3$  mg after drying) was subjected to further soaking in water and drying cycles, as described in the previous section, to eventually lead to the formation of phase pure enriched COM samples (Figures S4b and S5b).

**Storage of Enriched COM Phases.** All phase pure COM samples were stored in parafilm glass vials and placed in a container together with molecular sieves at  $-16$   $^\circ\text{C}$  until further use. Prior to any characterization by IR, pXRD, and ssNMR, samples were taken out of the freezer and left to thaw for 30 min.

**Preparation of Anhydrous Calcium Oxalate Mineral ( $^{17}\text{O}$ -COA).** Anhydrous calcium oxalate for  $^{17}\text{O}$  NMR studies was obtained by *in situ* dehydration of  $^{17}\text{O}$ -COM in the NMR instrument. The COM sample was packed in a 4 mm rotor (with the rotor sleeve and cap made of zirconia); the initial mass was 98.2 mg. The rotor was then introduced in a Bruker 4 mm WVT probe equipped with a Bruker booster BVTB 3500. Heating was performed using hot gas by progressively increasing the temperature up to 220  $^\circ\text{C}$ , while spinning at a frequency of 12 kHz. Nitrogen gas was used for the sample spinning to ensure no rehydration occurred during the cooling process back to room temperature. After the experiment, the rotor was removed from the magnet and immediately moved to the glove box (argon atmosphere), where it was transferred and repacked to a 2.5 mm rotor in view of further ssNMR experiments at 17.6 T.

**Characterization Techniques.** Infrared (IR) spectra were recorded on a PerkinElmer Spectrum 2 FT-IR instrument (optical resolution of 0.5  $\text{cm}^{-1}$ ) in attenuated total reflectance (ATR)

measurement mode. Analyses were performed in the 400–4000  $\text{cm}^{-1}$  range by averaging 4 acquisitions per sample.

Powder XRD (pXRD) analyses were performed on an X'Pert Pro diffractometer using  $\text{Cu K}\alpha_{1-2}$  radiation ( $\lambda = 1.5406/1.5444 \text{ \AA}$ ) with the operating voltage and current maintained at 40 kV and 25 mA, respectively. Diffractograms were recorded between 5 and 60° in  $2\theta$ , with a step size of 0.017° in approximately 8 min.

*In situ* pXRD analyses were performed under air on a Malvern-Panalytical Empyrean diffractometer with an Anton-Paar HTK16 high-temperature chamber using  $\text{Cu K}\alpha_{1-2}$  radiation ( $\lambda = 1.5406/1.5444 \text{ \AA}$ ). The data were collected between 5 and 50° in  $2\theta$ , with a step size of 0.013° and a total recording time of 50 min. The sample was suspended in ethanol and then deposited on a Pt–Rh (10%) strip. Ethanol was left to evaporate before starting the heat treatment. The heating rate was set to  $\sim 10 \text{ }^\circ\text{C}$  per minute, and once the desired temperature was reached, the diffraction powder pattern was recorded.

The pXRD analysis of the  $^{17}\text{O}$ -COA sample recovered after *in situ* NMR experiments was recorded on a Bruker D8 A25 machine using  $\text{Cu K}\alpha_{1-2}$  radiation ( $\lambda = 1.5406/1.5444 \text{ \AA}$ ). The data was collected between 17 and 60° in  $2\theta$ , with a step size of 0.025° and an effective detector counting time of 192 s.

High-resolution mass spectrometry (HRMS) analyses of enriched sodium oxalate samples were performed on a Synapt G2-S (Waters, SN: UEB205) mass spectrometer operating in a negative mode. Capillary and cone voltages were set to 3000 and 30 V, respectively. Source and desolvation temperatures were 250 and 100  $^\circ\text{C}$ , respectively. Data were processed using the MassLynx V4.2 software.<sup>41</sup> The HRMS analyses enabled an estimation of the enrichment level within the samples. For example, when using  $\sim 99\%$   $\text{H}_2^{18}\text{O}$  enriched water, the enrichment level was found to be  $\sim 45\%$ , while when using  $\sim 40\%$   $\text{H}_2^{17}\text{O}$ , it was  $\sim 19\%$  (Figure S6).

**Solid-State NMR Experiments.** ssNMR experiments were performed at multiple magnetic fields (9.4, 14.1, 17.6, 18.8, and 35.2 T) at different NMR facilities (ICGM in Montpellier, CEMHTI facility in Orléans, and NHMFL in Tallahassee). The spectra were acquired under magic-angle spinning (MAS) conditions with spinning frequencies varying from 4 to 30 kHz, and in some cases, using temperature regulation, as specified in Table S1. Chemical shifts were referenced as follows:  $^{17}\text{O}$  to tap water at 0.0 ppm (which corresponds to  $\text{D}_2\text{O}$  at ca.  $-2.7$  ppm,  $\text{D}_2\text{O}$  being the IUPAC recommended reference);<sup>42</sup>  $^{13}\text{C}$  to adamantane's high-frequency peak at 38.5 ppm [with respect to tetramethylsilane (TMS)].<sup>43</sup>

In some of the experiments listed below, SPINAL-64  $^1\text{H}$  decoupling<sup>44,45</sup> was applied during the evolution and/or acquisition period. The RF fields used for decoupling are given in Table S1.

**$^{17}\text{O}$  Solid-State NMR.** Part of the  $^{17}\text{O}$  NMR experiments were performed at 14.1 T on a Varian VNMRs spectrometer (ICGM), using 3.2 mm HX or HXY probes operating at  $^{17}\text{O}$  and  $^1\text{H}$  Larmor frequencies of 81.31 and 599.82 MHz, respectively. At this field, one-dimensional (1D)  $^{17}\text{O}$  MAS (Bloch decay) NMR spectra were recorded using a 1.0  $\mu\text{s}$  pulse for excitation (corresponding to a 22.5° tilt angle on a liquid).

At 17.6 T (CEMHTI), the  $^{17}\text{O}$  MAS NMR spectra were recorded on a Bruker Avance III HD NMR spectrometer equipped with a 2.5 mm probe operating at a  $^{17}\text{O}$  Larmor frequency of 101.70 MHz. The 1D  $^{17}\text{O}$  Hahn echo experiments were performed with one rotor period echo delay (33.33  $\mu\text{s}$ ), using  $\pi/2$  and  $\pi$  pulse lengths of 8 and 16  $\mu\text{s}$ , respectively. Two-dimensional (2D) multiple-quantum (MQ) MAS experiments were recorded with excitation, conversion, and central transition selective pulse lengths of 2.8, 1.1, and 7.5  $\mu\text{s}$ , respectively. To avoid rehydration of the anhydrous calcium oxalate phase (COA), ssNMR analyses were performed under  $\text{N}_2$  gas spinning; only a very weak  $^1\text{H}$  resonance (corresponding to water) was observed after 3 days of acquisition.

At 18.8 T (NHMFL),  $^{17}\text{O}$  MAS NMR experiments were performed on a Bruker Avance III HD 800 MHz NMR spectrometer using a 3.2 mm Low-E triple-resonance MAS probe operating at a  $^{17}\text{O}$  Larmor frequency of 108.47 MHz. 1D  $^{17}\text{O}$  experiments were recorded using a Bloch decay NMR pulse sequence, with an excitation pulse length of 3

$\mu\text{s}$ . 2D shifted-echo MQMAS spectra were acquired with excitation, conversion, and central transition selective pulse lengths of 3, 1, and 5  $\mu\text{s}$ , respectively. An additional 2D shifted-echo MQMAS with  $^{17}\text{O}\{^1\text{H}\}$  rotational echo double-resonance (REDOR) recoupling experiment<sup>46</sup> was performed using 8  $\mu\text{s}$   $\pi$  pulses on the  $^1\text{H}$  channel, with a total recoupling time of 0.5 ms.

At 35.2 T (NHMFL),  $^{17}\text{O}$  MAS NMR spectra were acquired on the Series Connected Hybrid (SCH) magnet,<sup>47</sup> using a Bruker Avance NEO NMR spectrometer equipped with a 3.2 mm single-resonance MAS probe operating at a  $^{17}\text{O}$  Larmor frequency of 203.36 MHz. The spinning frequency was set to 10 kHz with temperature control at +10  $^\circ\text{C}$ . The 1D  $^{17}\text{O}$  Hahn echo experiment was recorded using one rotor period echo delay, and  $\pi/2$  and  $\pi$  pulse lengths of 5.0 and 10.0  $\mu\text{s}$ , respectively. No  $^1\text{H}$  decoupling was applied for this experiment. 2D shifted-echo MQMAS experiments were recorded with excitation, conversion, and central transition selective pulse lengths of 3.3, 1.6, and 10  $\mu\text{s}$ , respectively. Because of possible instrumental interruptions such as magnet tripping at 35.2 T, these MQMAS experiments were recorded as four 2D acquisitions, which were then added together later for a better signal-to-noise ratio. The following equations<sup>48</sup> relate the chemical shift in the indirect dimension ( $\delta_1$ ) of MQMAS experiment to the isotropic chemical shift ( $\delta_{\text{iso}}$ ):

$$\delta_1 = \delta_{\text{iso}} - \frac{10}{17}\delta_{\text{qis}} \quad (1)$$

where the value of  $\delta_{\text{qis}}$  for  $I = 5/2$  is given by

$$\delta_{\text{qis}} = -6000 \times \frac{C_Q^2}{\nu_0^2} \left( 1 + \frac{\eta_Q^2}{3} \right) \quad (2)$$

In eq 2,  $C_Q$  is the quadrupolar coupling constant,  $\nu_0$  is the Larmor frequency, and  $\eta_Q$  is the asymmetry parameter.

Complementary information on all  $^{17}\text{O}$  ssNMR experiments can be found in the Supporting Information (SI, Table S1).

**$^{13}\text{C}$  NMR and  $^{13}\text{C}$ – $^{17}\text{O}$  Correlation NMR Experiments.** One-dimensional (1D)  $^{13}\text{C}$  ssNMR experiments were recorded on a VNMRs 14.1 T NMR spectrometer (ICGM), using a Varian 3.2 mm HX probe tuned to  $^1\text{H}$  and  $^{13}\text{C}$  (Larmor frequencies of 599.82 and 150.81 MHz, respectively). The spectra were acquired under MAS, using a cross-polarization (CP) sequence, with a 3.3  $\mu\text{s}$  excitation pulse on the  $^1\text{H}$  channel, followed by a ramped spin-lock pulse of 1.5 ms.

1D and 2D  $^{13}\text{C}/^{17}\text{O}$  MAS NMR experiments were recorded at the NHMFL on a Bruker Avance III HD 800 MHz (18.8 T) NMR spectrometer using a 3.2 mm Low-E probe in triple-resonance mode, tuned at frequencies of 201.19 ( $^{13}\text{C}$ ), 108.47 ( $^{17}\text{O}$ ) and 800.12 MHz ( $^1\text{H}$ ). The 1D cross-polarization magic-angle-spinning (CPMAS) experiment was recorded using 3  $\mu\text{s}$  pulse for  $^1\text{H}$  excitation, followed by a ramped contact pulse of 1.5 ms. A two-dimensional (2D) homonuclear  $^{13}\text{C}$  refocused INADEQUATE experiment with z-filter<sup>49</sup> was recorded using the same CP conditions as for the 1D  $^{13}\text{C}$  NMR experiment, with further  $^{13}\text{C}$   $\pi/2$  and  $\pi$  pulse lengths of 4 and 8  $\mu\text{s}$ , respectively.

2D heteronuclear  $^{13}\text{C}$ – $^{17}\text{O}$  MAS spectra were recorded at different temperatures using a MQ/D-RINEPT pulse sequence,<sup>50</sup> and SR4<sub>1</sub><sup>2</sup> dipolar recoupling.<sup>51</sup> The triple quantum (3Q) excitation, conversion, and central transition selective pulse lengths were 4, 1.4, and 5  $\mu\text{s}$ , respectively, followed by a D-RINEPT-based magnetization transfer with  $\pi/2$  and  $\pi$  pulse lengths of 4 and 8  $\mu\text{s}$ , respectively. The SR4<sub>1</sub><sup>2</sup>-based recoupling sequence was applied on the  $^{13}\text{C}$  channel.

***In Situ High-Temperature  $^{17}\text{O}$  and  $^{13}\text{C}$  NMR Experiments.*** The high-field *in situ* high-temperature 1D  $^{13}\text{C}$  and  $^{17}\text{O}$  MAS NMR experiments were recorded at 17.6 T (CEMHTI) on a Bruker Avance III HD spectrometer equipped with a 7.0 mm Bruker laser-heated MAS double-resonance probe operating at  $^1\text{H}$  and  $^{13}\text{C}$  (or  $^{17}\text{O}$ ) Larmor frequencies of 750.13 and 188.13 (or 101.70) MHz, respectively. A bottomless 7.0 mm MAS rotor was used, equipped with an inner aluminum nitride (AlN) container. Heating of the

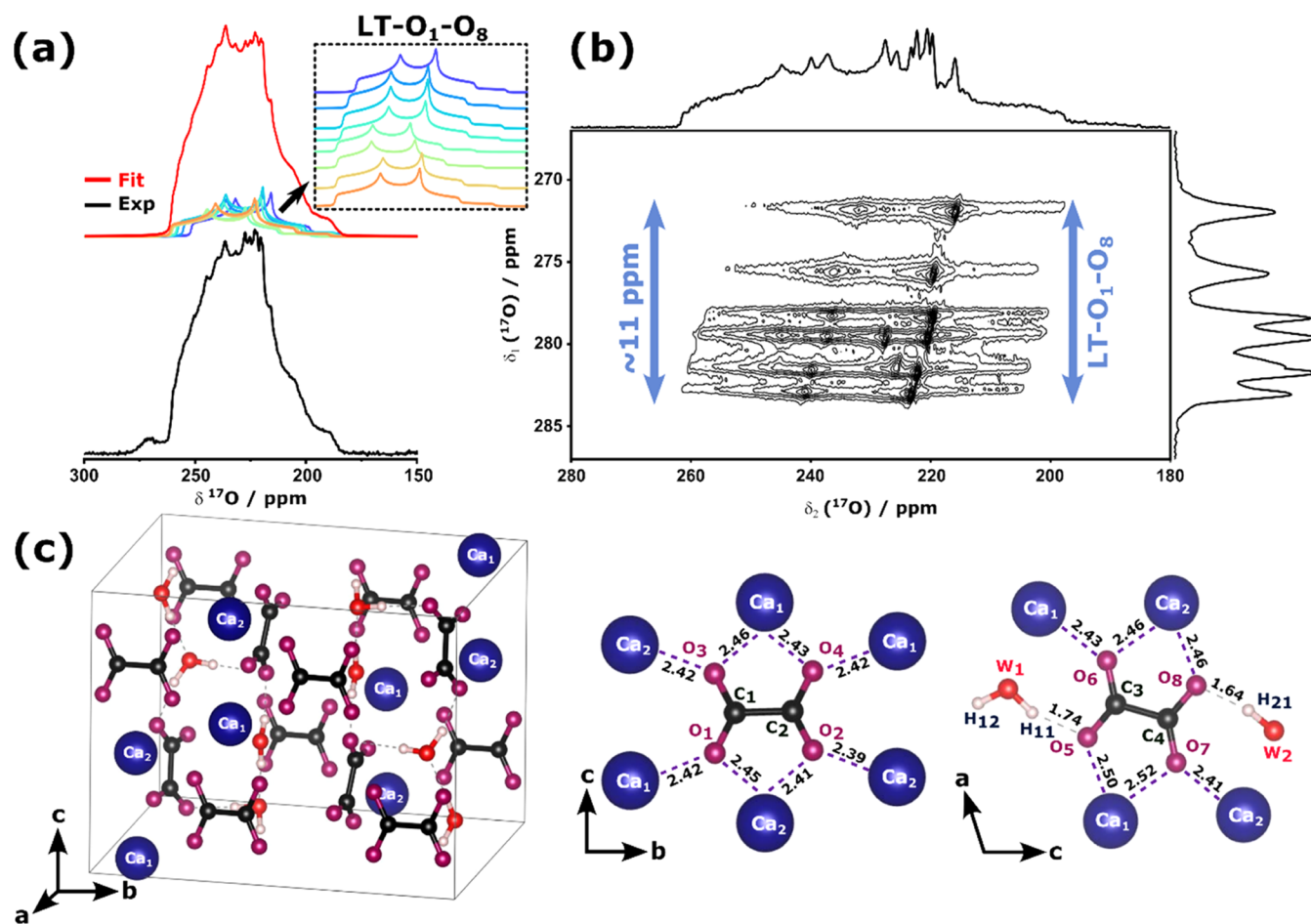


**Figure 2.** (a) 1D  $^{17}\text{O}$  MAS NMR spectrum of LT- $^{17}\text{O}$ -COM (in black), and its fit considering eight oxalate oxygen sites (in red); the inset shows the contribution from individual sites. (b) 2D  $^{17}\text{O}$  MQMAS NMR spectrum of the same sample showing 8 oxygen sites within an  $\sim 11$  ppm range (LT-O<sub>1</sub>-O<sub>8</sub>). Extracted slices and their fits can be found in the SI (Figure S10), and the NMR parameters of each site are reported in Table 1. Both spectra were recorded at 18.8 T, using a MAS frequency of 16 kHz; further experimental details are in Table S1. (c) Representations of the structure of LT-COM along different crystallographic orientations (with the same color code for atoms as in Figure 1); distances reported are those of the crystal structure (CCDC 1428017).<sup>54</sup>

sample was achieved using a 200 W DILAS diode laser operating at 980 nm up to 470 °C.<sup>52</sup> The temperature was calibrated using KBr and following the  $^{79}\text{Br}$  chemical shift change as a function of the laser power used.<sup>53</sup> *In situ* high-temperature 1D  $^{13}\text{C}$  MAS NMR experiments were recorded at a spinning speed of 4 kHz, using a single-pulse acquisition (Bloch decay) with a  $^{13}\text{C}$   $\pi/2$  pulse length of 7  $\mu\text{s}$ . At each temperature,  $^1\text{H}$  NMR experiments were performed to monitor the water signal and follow its decrease in intensity (spectra available on demand). At 220 °C, the sample was left spinning until no more  $^1\text{H}$  water signal was observed to ensure complete dehydration of the COM mineral, yielding an anhydrous phase.

Complementary *in situ* high-temperature experiments were recorded at 9.4 T (CEMHTI) on a Bruker Avance I NMR spectrometer equipped with a 4.0 mm WVT probe operating at  $^{17}\text{O}$  Larmor frequency of 54.18 MHz, and spinning at 12 kHz. 1D  $^{17}\text{O}$  DFS Hahn echo experiments were performed using a 1 ms DFS-pulse with a sweep between 200 kHz and 1 MHz, prior to the  $\pi/2$  and  $\pi$  pulses of the echo (8 and 16  $\mu\text{s}$ ), separated by an echo delay of one rotor period (83.3  $\mu\text{s}$ ). Additional  $T_1$  measurements were performed under 12 kHz MAS using a saturation recovery experiment at RT and 200 °C. The saturation recovery experiments were performed using  $\sim 100$  presaturation pulses (each 10  $\mu\text{s}$  long separated by 1 ms), followed by 5.5 and 11  $\mu\text{s}$   $\pi/2$  and  $\pi$  pulses, respectively. Following these analyses, the formed anhydrous COA sample was unpacked in the glove box and analyzed by pXRD, as mentioned above.

Nitrogen gas was used for spinning the rotors on both spectrometers to ensure no rehydration occurred during the experiment and the cooling process.

**Computational Studies.** The optimization of atomic positions for LT-COM was carried out starting from the crystallographic data reported by Daudon et al.,<sup>54</sup> as described elsewhere.<sup>36</sup> In brief, the geometry of the structure was optimized progressively: first, proton positions, then oxygen atoms directly bonded to hydrogen atoms, and finally, all atoms.

A model of the relaxed HT-COM structure (supercell size of  $2 \times 2 \times 2$ ) was kindly provided by Shepelenko and co-workers (Weizmann Institute of Science) to deal with the partial occupancies of the experimental structure (see Figure S7 in the SI for a representation of the supercell).

The crystal structure of the anhydrous calcium oxalate ( $\alpha$ -polymorph) was taken from the work by Izatulina et al. (CCDC 1846250).<sup>17</sup> Atomic positions were relaxed using the Vienna *Ab initio* Simulation Package (VASP),<sup>55,56</sup> based on the Kohn–Sham DFT, and using a plane-wave pseudopotential approach with an energy cutoff of 400 eV, and a  $2 \times 3 \times 4$   $k$ -point mesh for the anhydrous phase. During the geometry optimization, unit cell parameters were kept fixed.

NMR parameters were calculated for all structures using the QUANTUM-ESPRESSO code,<sup>57</sup> keeping the atomic positions equal to the values previously determined using VASP. The Perdew–Burke–Ernzerhof (PBE) generalized gradient approximation was

**Table 1. Average Experimental  $^{17}\text{O}$  NMR Parameters for All Oxygen Sites of LT, HT- $^{17}\text{O}$ -COM, and  $^{17}\text{O}$ -COA Samples Studied in This Work<sup>a</sup>**

compound (figure)	$\delta_{\text{iso}}$ (ppm)	$ C_Q $ (MHz)	$\eta_Q$	assignment	magnetic fields (T)
LT- $^{17}\text{O}$ -COM (Figure 2)	$254.1 \pm 0.1$	$7.27 \pm 0.02$	$0.52 \pm 0.01$	LT-O <sub>7</sub>	9.4, 14.1 and 18.8
	$258.3 \pm 0.3$	$7.30 \pm 0.02$	$0.50 \pm 0.01$	LT-O <sub>6</sub>	
	$259.9 \pm 0.2$	$7.41 \pm 0.04$	$0.53 \pm 0.01$	LT-O <sub>1</sub> /O <sub>3</sub>	
	$260.8 \pm 0.1$	$7.45 \pm 0.01$	$0.53 \pm 0.01$	LT-O <sub>2</sub> /O <sub>4</sub>	
	$262.9 \pm 0.2$	$7.49 \pm 0.02$	$0.51 \pm 0.01$	LT-O <sub>1</sub> /O <sub>3</sub>	
	$263.9 \pm 0.1$	$7.50 \pm 0.01$	$0.50 \pm 0.01$	LT-O <sub>2</sub> /O <sub>4</sub>	
	$264.0 \pm 0.4$	$7.07 \pm 0.03$	$0.45 \pm 0.01$	LT-O <sub>8</sub>	
	$264.8 \pm 0.6$	$7.31 \pm 0.04$	$0.40 \pm 0.01$	LT-O <sub>5</sub>	
HT- $^{17}\text{O}$ -COM (Figure 5)	$256.0 \pm 0.5$	$7.13 \pm 0.02$	$0.55 \pm 0.01$	HT-O <sub>11</sub>	9.4, 14.1, 17.6 and 18.8
	$262.8 \pm 0.4$	$7.49 \pm 0.01$	$0.52 \pm 0.01$	HT-O <sub>9</sub>	
	$264.4 \pm 0.5$	$7.12 \pm 0.01$	$0.50 \pm 0.01$	HT-O <sub>10</sub>	
$^{17}\text{O}$ -COA (Figure 6)	$242.6 \pm 0.1$	$6.96 \pm 0.10$	$0.74 \pm 0.01$	A-O <sub>15</sub>	17.6 and 9.4
	$256.3 \pm 0.1$	$7.47 \pm 0.05$	$0.49 \pm 0.01$	A-O <sub>12</sub> /O <sub>13</sub>	
	$261.7 \pm 0.1$	$7.47 \pm 0.01$	$0.52 \pm 0.01$	A-O <sub>12</sub> /O <sub>13</sub>	
	$282.4 \pm 0.1$	$7.88 \pm 0.08$	$0.24 \pm 0.01$	A-O <sub>14</sub>	

<sup>a</sup>See Figures S9, S10, S14, S15, S19, and S20 for the experimental spectra and multifield fits, and Table S1 for experimental acquisition parameters.

used,<sup>58</sup> and the valence electrons were described by norm-conserving pseudopotentials<sup>59</sup> in the Kleinman-Bylander form.<sup>60</sup> The shielding tensor was computed using the GIPAW approach.<sup>61</sup> The wave functions were expanded on a plane-wave basis set with a kinetic energy cutoff of 80 Ry. The calculations were done using a *k*-space mesh density of  $\sim 0.04 \text{ \AA}^{-1}$ .

The isotropic chemical shift  $\delta_{\text{iso}}$  is defined as  $\delta_{\text{iso}} \approx -(\sigma_{\text{iso}} - \sigma_{\text{ref}})$ , where  $\sigma_{\text{iso}}$  is the isotropic shielding and  $\sigma_{\text{ref}}$  is the isotropic shielding for the same nucleus in a reference system.<sup>62</sup> Different structures were selected to establish a relevant reference chemical shift for  $^{17}\text{O}$  (Table S2). In this work, the value used for  $\sigma_{\text{ref}}$  was 228 ppm (slope kept at  $-1$ ; Figure S8). This  $\sigma_{\text{ref}}$  value was derived from comparisons between the calculated shieldings ( $\sigma_{\text{iso}}$ ) with experimental isotropic shifts ( $\delta_{\text{iso}}$ ), for a selection of compounds involving Ca $\cdots$ O and/or C–O bonds, as present in the Ca-oxalate structures studied here. The list of reference structures (amino acids, oxalic acid, calcite, and wollastonite) and their  $^{17}\text{O}$  NMR parameters are reported in Tables S2 and S3. It is important to highlight that the inclusion of several oxygen environments involving Ca $\cdots$ O bonds was found to be essential to account for the partial Ca-3d O-2p hybridization,<sup>63</sup> and for establishing a “reasonable” value of  $\sigma_{\text{ref}}$  to be used for NMR calculations on Ca-oxalates (as here our Ca pseudopotential used was not corrected for this effect). Indeed, when using previously reported  $\sigma_{\text{ref}}$  values (e.g.,  $\sim 260$  ppm), calculated  $^{17}\text{O}$  chemical shifts for oxalate oxygen atoms were systematically off by more than 30 ppm.<sup>36,64</sup>

The quadrupolar moments (*Q*) used to calculate the  $^{17}\text{O}$  quadrupolar coupling constant  $C_Q$  was  $-2.558 \text{ fm}^2$ .<sup>65</sup> Regarding the chemical shift anisotropy (CSA) parameters, we used here Herzfeld–Berger convention.<sup>66</sup> Further terminology and definitions for chemical shift and quadrupolar parameters are given in the SI and previous work.<sup>36</sup>

Molecular dynamics (MD) simulations were carried out with the CP2K code<sup>67</sup> consisting in Born–Oppenheimer MD (BOMD) with PBE electronic representation, including the Grimme (D3) correction for dispersion,<sup>68</sup> GTH pseudopotentials,<sup>69</sup> combined plane-wave, and TZVP basis sets.<sup>70</sup> The BOMD was performed using the NVT ensemble, and Nosé–Hoover thermostat was used to control the average temperature at 300 or 320 K. Trajectories were accumulated over  $\sim 4$  ps with a time step of 0.5 fs, and  $^{17}\text{O}$  NMR calculations were performed with QE, with averaging done every 100 or 200 steps, i.e., every 50 or 100 fs, for 300 and 320 K, respectively.

All calculated structures as well as further computational details are available upon reasonable demand.

All spectra which had been recorded on a Varian VNMRs console were converted to the TOPSPIN software (<https://www.bruker.com/en.html>) and further processed there. Depending on the experiment, an exponential line broadening was applied to the spectra prior to the

Fourier transform. To extract quadrupolar and chemical shift parameters,  $^{17}\text{O}$  MAS NMR spectra were fitted using the ssNAKE software.<sup>71</sup> 2D  $^{17}\text{O}$  MQMAS spectra recorded at 35.2 T were summed for a better signal-to-noise ratio using a MATLAB<sup>72</sup> script written by I. Hung.

## RESULTS AND DISCUSSION

**High-Resolution  $^{17}\text{O}$  ssNMR of LT- $^{17}\text{O}$ -COM: Monitoring the Diversity of Oxalate Binding Environments.** To explore calcium oxalate phase transitions via oxygen- $^{17}\text{O}$  ssNMR, an isotopically enriched version of LT-COM was synthesized, using  $^{17}\text{O}$ -labeled oxalate ligands prepared by mechanochemistry (Scheme 1). For the first experiments,  $\sim 40\%$   $^{17}\text{O}$ -enriched water was used in the labeling step, leading to an average enrichment level  $\sim 19\%$  per oxygen, according to HRMS (Figure S6). The  $^{17}\text{O}$  MAS ssNMR spectrum of LT- $^{17}\text{O}$ -COM is presented in Figure 2a. The high enrichment level of the oxalate oxygen atoms within this sample resulted in excellent sensitivity, allowing the spectrum to be recorded in less than 6 min at 18.8 T. The  $^{17}\text{O}$  resonances were detected in the spectral region characteristic of carboxylate groups,<sup>28–32</sup> but with no direct resolution over the eight inequivalent oxalate oxygen sites expected from the LT-COM crystal structure, due to the quadrupolar broadening.

To achieve higher resolution, a 2D MQMAS experiment was performed (Figure 2b). All oxalate sites could thus be resolved, as shown by looking at the spectra of the different “slices” and their individual fits (see Figure S9).  $^{17}\text{O}$  MAS NMR spectra of LT-COM were then recorded at different magnetic fields (9.4, 14.1, and 18.8 T) and fitted (Figure S10). The extracted average chemical shift ( $\delta_{\text{iso}}$ ) values and quadrupolar parameters ( $C_Q$  and  $\eta_Q$ ) for each site are reported in Table 1. The chemical shift range was found to span over only 11 ppm for these eight inequivalent sites (between 254 and 265 ppm).  $C_Q$  and  $\eta_Q$  values were also very similar, ranging from 7.1 to 7.5 MHz in the former case, and from 0.40 to 0.53 in the latter. A complementary MQMAS analysis was carried out at ultrahigh magnetic field (35.2 T) to extract the CSA parameters  $\delta_{\text{cs}}$  and  $\eta_{\text{cs}}$  of individual sites (Figure S11 and Table S4). Despite the uncertainties related to some peaks overlapping at this magnetic field, similar values were again found for all sites,

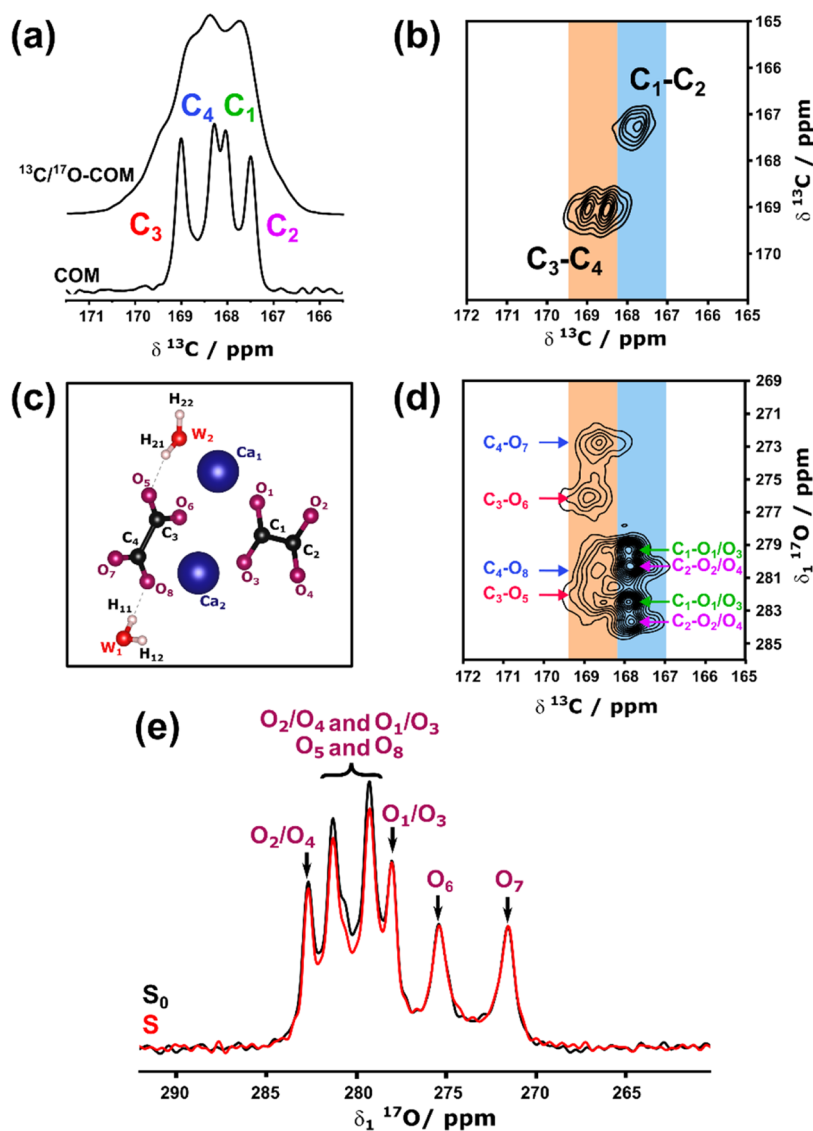


**Figure 3.** (a)  $^{13}\text{C}$  1D CPMAS spectra of LT-COM at natural abundance (bottom) and for the doubly enriched  $^{13}\text{C}/^{17}\text{O}$  phase (top). (b) Homonuclear 2D  $^{13}\text{C}$ – $^{13}\text{C}$  INADEQUATE at +20 °C with the assignment of the carbon signals (as proposed according to Colas et al.<sup>73</sup>). (c) Crystal structure of LT-COM as reported by Daudon et al.<sup>54</sup> (d) 2D heteronuclear  $^{13}\text{C}$ – $^{17}\text{O}$  MQ/D-RINEPT spectrum of  $^{13}\text{C}/^{17}\text{O}$ -LT-COM recorded at +20 °C with a tentative assignment of the cross-peaks. The chemical shifts and assignments derived from spectra (b) and (d) are reported in Table 2. The differences in relative intensities of the cross-peaks probably reflect differences in J couplings. (e) Indirect dimension ( $\delta_1$ ) of the MQMAS  $^{17}\text{O}\{^1\text{H}\}$  MQ/REDOR experiment carried out on LT- $^{17}\text{O}$ -COM, recorded with (in red) and without (in black)  $^1\text{H}$ -recoupling. The dephasing time used here was 0.5 ms.

with estimated  $\delta_{\text{CS}}$  between  $-163$  and  $-200$  ppm, and  $\eta_{\text{CS}}$  between 0.6 and 0.9.

As previous ssNMR analyses of COM had shown the usefulness of *ab initio* calculations to help rationalize the experimental NMR spectra,<sup>36,73,74</sup> DFT-GIPAW calculations were carried out, focusing on the  $^{17}\text{O}$  NMR parameters of oxalate oxygen atoms (Table S5). No straightforward one-to-one correlation between experimental and calculated parameters for the different sites could be established. The absolute values of the calculated quadrupolar coupling constants were systematically higher than the experimental ones, reaching  $\sim 8.2$  MHz for several sites (up to  $\sim 1$  MHz more than some experimental values). Similarly, the calculated  $\delta_{\text{iso}}$  values were found to span over  $\sim 14$  ppm, instead of 11 ppm experimentally. The calculated absolute values of  $\delta_{\text{CS}}$  were also found to be, on average,  $\sim 80$  ppm higher compared to the

experimentally determined ones (Tables S4 and S5). Such discrepancies between the calculated and experimental parameters can be explained by the lack of inclusion of dynamics within these calculations: DFT calculations are carried out at 0 K considering no molecular motions of atoms, while the experimental data was recorded close to room temperature. As shown for other systems, local atomic/molecular motions within the lattice (notably of the nearby water molecules) can lead to the averaging of the electronic environments of oxalate oxygen atoms and partial averaging of NMR parameters.<sup>30,36,75,76</sup> Preliminary molecular dynamics (MD) simulations were thus carried out at 300 K, followed by GIPAW-DFT calculations of structures extracted along the MD steps, to see how motions within the LT-COM lattice affect the  $^{17}\text{O}$  parameters of the oxalate oxygen atoms. As shown in Figure S12, the resulting calculated  $\delta_{\text{iso}}$  and  $C_{\text{Q}}$  values

at 300 K were found to differ from those at 0 K, with the extent of variation depending upon the oxygen site considered. Yet, the relative order of these calculated  $\delta_{\text{iso}}$  values was still inconsistent with our LT-COM experimental assignments. Hence, the influence of smaller changes in temperature was investigated by performing a similar MD simulation at 320 K. This led to further changes in some of the relative orders of  $\delta_{\text{iso}}$  and  $C_Q$  of the different sites. Overall, such calculations clearly point to a strong dependence of the oxalate  $^{17}\text{O}$  NMR parameters on temperature, as described later in the manuscript, and further underscores the importance of being able to perform experimental assignments of the oxalate resonances.

To help gain resolution, a doubly labeled sample (enriched in  $^{13}\text{C}$  and  $^{17}\text{O}$ ) was prepared. The LT- $^{13}\text{C}/^{17}\text{O}$ -COM phase was synthesized starting from 99%  $^{13}\text{C}$ -labeled diethyl oxalate (enriched on both carboxyl carbon atoms) and using  $\sim 90\%$   $\text{H}_2^{17}\text{O}$  for the mechanochemical saponification step, leading to an average  $^{17}\text{O}$ -enrichment level ca. 40–45% on the oxalate oxygen atoms (as estimated from our previous experience on such labeling reactions).<sup>38,40</sup> First, the 1D  $^{13}\text{C}$  NMR spectrum was recorded (Figure 3a, top). Due to the very high  $^{13}\text{C}$ -enrichment level in LT- $^{13}\text{C}/^{17}\text{O}$ -COM, the spectrum is significantly broadened compared to the nonenriched COM phase (Figure 3a, bottom) due to the J coupling and  $n \sim 0$  rotational resonance of the dipolar coupling between two  $^{13}\text{C}$  with close isotropic shifts, but different CSA tensor orientations. While four resonances are resolved in the one-dimensional  $^{13}\text{C}$  CPMAS NMR spectrum of nonlabeled LT-COM at 20 °C (with the inequivalent carbon sites assigned as proposed by Colas et al.),<sup>73</sup> high resolution in  $^{13}\text{C}$  could only be achieved in the case of the doubly labeled LT- $^{13}\text{C}/^{17}\text{O}$ -COM phase by using a two-dimensional homonuclear  $^{13}\text{C}$ – $^{13}\text{C}$  INADEQUATE experiment (Figure 3b). Indeed, the two sets of signals corresponding to the two inequivalent oxalate ions are thus resolved (Figure 3b), where the higher-frequency signals correspond to  $C_3$  and  $C_4$ , and the lower ones to  $C_1$  and  $C_2$  (Table 2 and Figure 3c). Subsequently, the doubly labeled phase was studied using a 2D heteronuclear  $^{13}\text{C}$ – $^{17}\text{O}$  MQ/D-RINEPT experiment. The SR4<sub>2</sub><sup>1</sup> dipolar recoupling scheme was used, with a short recoupling time, so that the cross-peaks correspond to the directly bound  $^{13}\text{C}$ – $^{17}\text{O}$  atoms.<sup>51</sup> The four oxygen atoms belonging to each inequivalent oxalate ion were thus separated, as shown in

**Table 2. Chemical Shifts and Proposed Assignment of  $\delta_1^{13}\text{C}$  and  $\delta_1^{17}\text{O}$  Resonances, as Shown in Figures 2 and 3<sup>a</sup>**

2D $^{13}\text{C}$ – $^{13}\text{C}$ INADEQUATE		$^{13}\text{C}$ – $^{17}\text{O}$ MQ/D-RINEPT SR4 <sub>2</sub> <sup>1</sup> and $^{17}\text{O}\{^1\text{H}\}$ MQ/REDOR	
$\delta_{\text{iso}}/\text{ppm}$ ( $\delta^{13}\text{C}$ )	assignment	$\delta_1/\text{ppm}$ ( $\delta_1^{17}\text{O}$ )	assignment
168.9	C3	275.1	O <sub>6</sub>
		281.5	O <sub>5</sub>
168.7	C4	271.8	O <sub>7</sub>
		279.6	O <sub>8</sub>
167.9	C1	278.3	O <sub>1</sub> /O <sub>3</sub>
		281.5	
167.7	C2	279.3	O <sub>2</sub> /O <sub>4</sub>
		282.7	

<sup>a</sup> $\delta_1^{17}\text{O}$  ( $^{17}\text{O}$ ) is a chemical shift in the indirect dimension of the 2D MQMAS experiment, which differs from  $\delta_{\text{iso}}^{17}\text{O}$  ( $^{17}\text{O}$ ) (see the Experimental Section for details on how  $\delta_1$  is calculated and related to  $\delta_{\text{iso}}$ ).

Figure 3d, where the beige and blue-shaded zones correspond to the signals arising from the two different oxalate ions. This enabled us to determine, for each of the 4 inequivalent oxalate carbon atoms, which two oxygen resonances correspond to the atoms directly linked to them (Table 2). Further discrimination between the two oxygen atoms bound to the same carbon (e.g., O<sub>5</sub> vs O<sub>6</sub>, or O<sub>7</sub> vs O<sub>8</sub>), was achieved by probing the  $^{17}\text{O}\cdots^1\text{H}$  proximities in LT- $^{17}\text{O}$ -COM using 2D MQMAS in combination with  $^{17}\text{O}\{^1\text{H}\}$ -REDOR. According to the crystal structure (Figure 3c), O<sub>5</sub> and O<sub>8</sub> are involved in hydrogen bonding, while O<sub>6</sub> and O<sub>7</sub> are not (nor O<sub>1</sub> to O<sub>4</sub>), meaning that the former oxygen sites should be distinguishable on the basis of their higher  $^{17}\text{O}\cdots^1\text{H}$  dipolar couplings, i.e., proximities. Figure 3e shows a comparison of the  $^{17}\text{O}$   $\delta_1$  dimension of the  $^{17}\text{O}\{^1\text{H}\}$  MQ/REDOR experiment, performed without (black) and with (red)  $^1\text{H}$  recoupling of 0.5 ms. No change in the signal intensities was observed for the two lower-frequency resonances (centered at 271.8 and 275.1 ppm), while a small amount of dephasing is noticeable for signals in the range between 277 and 285 ppm, implying that O<sub>5</sub> and O<sub>8</sub> are in the higher shift zone (Table 2). (Here, it is the  $\delta_1^{17}\text{O}$  values that are considered, which differ from  $\delta_{\text{iso}}^{17}\text{O}$ ), as detailed in the experimental section). Although a more complete assignment of each of the oxygen resonances of the other oxalate ligand (blue-shaded zone) could not be performed at this stage, it should nevertheless be highlighted that this is the first time that  $^{17}\text{O}$  NMR spectra showing the oxalate resonances of LT-COM are reported, with the eight oxygen sites being fully resolved using  $^{17}\text{O}$  MQMAS and  $^{13}\text{C}$ – $^{17}\text{O}$  MQ/D-RINEPT experiments. This is all the more noteworthy considering the similar oxygen local environments and the small isotropic chemical shift range of only  $\sim 11$  ppm. Thus, it demonstrates the potential of high-resolution  $^{17}\text{O}$  NMR for finely investigating the structure of oxalate-based materials. Following these first results, we then decided to look into the successive phase transitions of LT-COM upon heating, focusing on the signatures of the oxalate oxygen atoms.

**Phase Transition from LT- to HT-COM: Following Progressive Changes in Oxalate Local Environments.** As mentioned in the Introduction section (Figure 1), upon heat treatment up to  $\sim 75$  °C, LT-COM gradually transforms into HT-COM. The latter phase has a different lattice symmetry and presents a positional disorder on the water molecules and some of the oxalate oxygen atoms, based on XRD analyses and computational studies.<sup>17,20</sup> Moreover, recently, we showed using  $^{17}\text{O}$  and  $^2\text{H}$  ssNMR that the water molecules progressively undergo more pronounced molecular motions when transitioning to the HT form.<sup>36</sup> Regarding the oxalate local environments,  $^{13}\text{C}$  CPMAS NMR analyses at natural abundance have shown that the 4 resolved inequivalent carbon sites of LT-COM merge into two main resonances upon heat treatment,<sup>26</sup> which is in line with the formation of an HT-COM phase with  $I2/m$  (equivalent to  $C2/m$ ) symmetry.<sup>20</sup> Here, to follow the transition from the LT- to the HT-COM form more precisely, we performed for the first time variable-temperature  $^{17}\text{O}$ – $^{13}\text{C}$  ssNMR analyses, by looking directly at the local environments of the oxalate oxygens (Figure 4).

The 2D  $^{13}\text{C}$ – $^{17}\text{O}$  MQ/D-RINEPT NMR spectra of the doubly labeled  $^{13}\text{C}/^{17}\text{O}$ -COM sample were recorded at four different temperatures between  $-30$  and  $+75$  °C, as shown in Figure 4. From the  $^{13}\text{C}$  perspective, the merging of the  $^{13}\text{C}$  resonances of each oxalate group (i.e.,  $C_1$  and  $C_2$  on one hand,

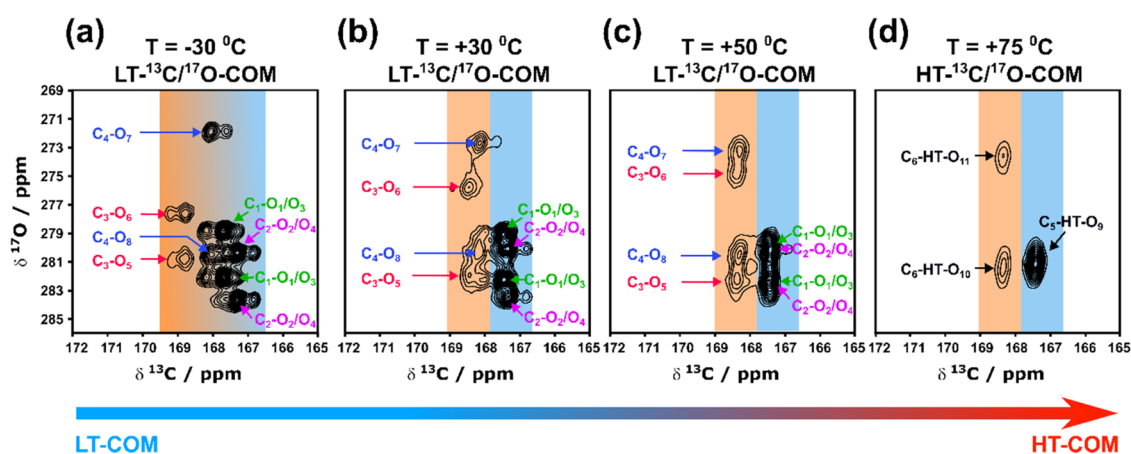


**Figure 4.** 2D heteronuclear  $^{13}\text{C}$ – $^{17}\text{O}$  MQ/D-RINEPT spectra recorded at (a)  $-30$ , (b)  $+30$ , (c)  $+50$ , and (d)  $+75$   $^{\circ}\text{C}$ , showing the evolution of oxygen and carbon sites with increasing temperature. Table S6 shows how chemical shifts are evolving with respect to temperature. The combined contributions of J, dipolar, and quadrupolar couplings give rise to the asymmetric appearance of the  $^{13}\text{C}$ – $^{17}\text{O}$  correlations in the 2D spectra. At higher temperatures, the asymmetry seems to be reduced in intensity due to increased dynamics. The differences in relative intensities of the main cross-peaks probably reflect differences in the  $^{13}\text{C}$ – $^{17}\text{O}$  J couplings. Oxygen sites abbreviated in this article as  $\text{O}_9$ ,  $\text{O}_{10}$ , and  $\text{O}_{11}$  correspond to  $\text{O}_{11}$ ,  $\text{O}_{13}/\text{O}_{14}$ , and  $\text{O}_9$ , respectively, in the reported crystal structure by Shepelenko et al.<sup>20</sup>

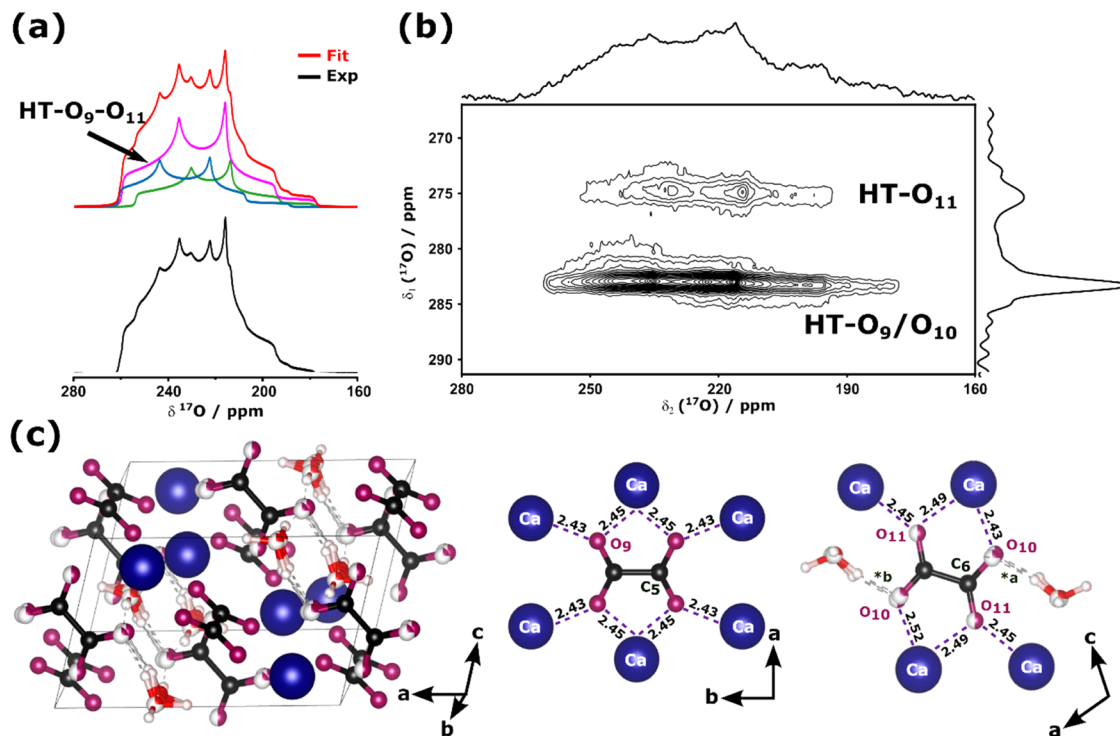


**Figure 5.** (a) 1D  $^{17}\text{O}$  MAS NMR spectrum of HT-COM- $^{17}\text{O}$  (in black), together with its fit considering three oxalate oxygen sites (in red); the individual contributions from sites  $\text{O}_9$ ,  $\text{O}_{10}$ , and  $\text{O}_{11}$  (in pink, blue, and green, respectively). (b) 2D  $^{17}\text{O}$  MQMAS NMR spectrum of the same sample showing three oxygen sites. Extracted slices with corresponding fits can be found in the SI (Figure S14), while the NMR parameters of each site are in Table 1. Both spectra were recorded at 17.6 T, using a MAS frequency of 30.3 kHz at  $+80$   $^{\circ}\text{C}$ . For further experimental details, see Table S1. (c) Representation of the crystal structure of HT-COM, showing the different average orientations of the water molecules in the lattice. Distances reported come from the published crystal structure of Shepelenko et al.<sup>20</sup> Distances noted \*a and \*b vary from 1.63 to 2.24 Å and from 1.63 to 2.39 Å, respectively.

and  $\text{C}_3$  and  $\text{C}_4$  on the other) is observed above  $+50$   $^{\circ}\text{C}$ , leading to the two resolved  $^{13}\text{C}$  resonances (noted here  $\text{C}_5$  and  $\text{C}_6$ —but which correspond to  $\text{C}_5$  and  $\text{C}_{11}$ , respectively, in the initially reported crystal structure by Shepelenko et al.), as expected from previously reported 1D  $^{13}\text{C}$  CPMAS NMR analyses<sup>26</sup> of HT-COM (see the evolution of the  $^{13}\text{C}$  as a function of the temperature in Figure S13). From the  $^{17}\text{O}$  perspective, it is also possible to follow the oxygen chemical shift changes with

respect to the different temperatures. Indeed, a partial merging of the  $^{17}\text{O}$  resonances of  $\text{O}_5$  with  $\text{O}_8$  (leading to  $\text{O}_{10}$  in HT-COM), of  $\text{O}_6$  with  $\text{O}_7$  (leading to  $\text{O}_{11}$  in HT-COM), and of the  $\text{O}_1$ – $\text{O}_4$  signals ( $\text{O}_9$  in HT-COM) is observed. Notably, the  $\text{O}_6$  position moves significantly to lower  $\delta_{\text{iso}}(^{17}\text{O})$  chemical shift values with temperature (comparing  $-30$  and  $+50$   $^{\circ}\text{C}$  data), which is consistent with the evolution of the calculated chemical shift value of this specific site comparing static 0 K

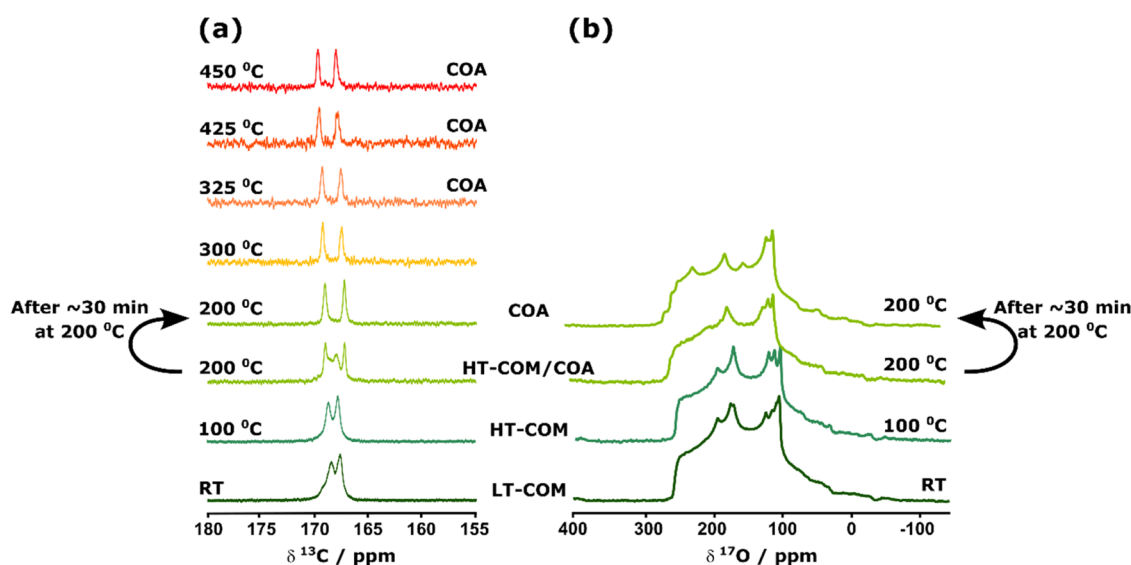


**Figure 6.** (a) 1D  $^{13}\text{C}$  MAS NMR spectra recorded at different temperatures at 17.6 T on the  $^{13}\text{C}$ -COM sample (using a 7 mm rotor). (b) 1D  $^{17}\text{O}$  MAS NMR experiments recorded at 9.4 T on the  $^{17}\text{O}$ -COM sample (using a 4 mm rotor). The  $^{17}\text{O}$  NMR spectrum of the COA phase was rerecorded after cooling back to room temperature under  $\text{N}_2$  gas flow, showing no change.

(Table S5) and MD averaged results (Figure S12). Such analyses demonstrate the importance of  $^{17}\text{O}$  ssNMR. The changes in  $^{17}\text{O}$  NMR shifts are more pronounced upon heat treatment than the  $^{13}\text{C}$  ones, making it a very sensitive probe to local binding environments. Moreover, while two  $^{13}\text{C}$  resonances are resolved for the inequivalent oxalates of HT-COM ( $\text{C}_5$  and  $\text{C}_6$ ), three  $^{17}\text{O}$  resonances can be distinguished for their oxygens [i.e., two for oxygen atoms coordinated to  $\text{Ca}^{2+}$  only ( $\text{O}_9$  and  $\text{O}_{11}$ ), and one coordinated to  $\text{Ca}^{2+}$  and involved in H-bonds with water molecules ( $\text{O}_{10}$ )]. Hence,  $^{17}\text{O}$  ssNMR stands out as a key asset for analyzing crystalline phases involving oxalate ligands in detail by “NMR crystallography”, providing direct insight into different oxygen local vicinities.

Complementary high-resolution  $^{17}\text{O}$  NMR analyses of the HT-COM structure were then performed to determine the quadrupolar parameters for the three inequivalent oxygen sites resolved at +75 °C (Figure 4d). The 1D  $^{17}\text{O}$  MAS and 2D MQMAS NMR spectra are shown in Figures 5, S14, and S15. The fitted NMR parameters extracted from the multiple magnetic field analyses are given in Table 1. Assignments were performed considering both the relative intensity and the  $^{17}\text{O}$  chemical shifts of the 3 sites observed at 75 °C (Figure 4d). Overall, the chemical shift range for the HT-COM structure was found to be slightly smaller compared to the LT-COM one, spanning from 256 to 264 ppm. The quadrupolar parameters were similar, with  $C_Q$  between 7.1 and 7.5 MHz, and  $\eta_Q$  between 0.50 and 0.55 (Table 1).

These high-resolution  $^{17}\text{O}$  NMR analyses of oxalates in HT-COM provide information about its structure, which is complementary to what was reported in our previous work.<sup>36</sup> First, while the  $^{17}\text{O}$  ssNMR spectra of the water molecules in HT-COM had shown a loss in quadrupolar line shape (which could be explained by the increased dynamics of these molecules at high temperature), the oxalate  $^{17}\text{O}$  NMR parameters and line shapes of the HT form remain close to those of the LT one. Hence, within the time scale probed by these NMR experiments, it appears that molecular motions within the HT-COM structure are essentially centered around

the water molecules. The progressive merging of the oxalate  $^{13}\text{C}$  and  $^{17}\text{O}$  signals with temperature (Figure 4) then attests only to increased local atomic motions within the HT-lattice, which results in some of the environments of oxalate oxygens becoming equivalent upon heating (due to resulting distance and angle averaging around them), and in a change in crystal symmetry upon heat treatment. Interestingly, it can be noted that the  $^{17}\text{O}$  quadrupolar coupling constants of  $\text{O}_{10}$  and  $\text{O}_{11}$  are  $\sim 0.3$  MHz smaller than for  $\text{O}_9$ , which may reflect the fact that the former oxygen sites are in closer proximity to the water molecules and, hence, more sensitive to their movements, leading to a more “averaged”  $^{17}\text{O}$  electronic environment for the nearby oxalate oxygen atoms.

In order to go further in the study of the structure and dynamics within HT-COM, and account for all ssNMR observations, a more complete computational study would be required, involving both MD simulations and *ab initio* calculations of NMR parameters using the GIPAW method.<sup>77</sup> Yet, calculations on the HT form are more computationally demanding than on the LT form, due to the change in symmetry at high temperature, implying the need to work on a supercell for HT-COM (Figure S7b). Although preliminary GIPAW-DFT calculations were performed on this structure at 0 K (see Table S7 and Figure S16), comprehensive investigations were not performed at this stage.

**Formation and Characterization of Anhydrous Calcium Oxalate.** Upon further heating, COM undergoes dehydration, leading to the formation of anhydrous calcium oxalate (COA, Figure 1). To date, three anhydrous polymorphs have been reported (noted  $\alpha$ ,  $\beta$ , and  $\gamma$ ), and their structure, formation, and interconversion have been studied both experimentally and computationally.<sup>17,18,33</sup> Using *in situ* pXRD analyses, it was proposed that the  $\alpha$  form appears first in the 120–150 °C range, followed by  $\beta$  around ca. 310–340 °C, and finally  $\gamma$  at  $\sim 410$  °C.<sup>17</sup> Yet, the exact temperature of appearance of these polymorphs was found to depend on the heating conditions and the nature of the experimental setups used (e.g., sample in a capillary or on a platinum strip).<sup>17,33</sup> Moreover, controversial conclusions about the structure of the transient  $\alpha$  polymorph



a significant change in the oxygen-17 line shape was observed, attesting to COA formation. After cooling the COA sample back to room temperature under N<sub>2</sub> gas (to avoid any rehydration), further analyses were performed at 17.6 T using 1D and 2D MQMAS experiments to resolve the oxygen sites. As shown in Figure 7, four oxygen sites were thus resolved in the <sup>17</sup>O-COA phase (Figure S19). The multifield fits of this sample are presented in Figure S20, together with the integrated relative intensities for each site, and their <sup>17</sup>O NMR parameters are reported in Table 1.

Because anhydrous calcium oxalate can exist as different polymorphs, complementary pXRD analyses were performed to help identify the anhydrous <sup>17</sup>O-COA phase(s) which had been isolated by progressive dehydration of <sup>17</sup>O-COM in the ssNMR probe, and characterized by high-resolution <sup>17</sup>O NMR. First, following the ssNMR analyses, the pXRD pattern of the sample was recorded under inert atmosphere: it was found to match the one of the  $\alpha$ -polymorph (Figure S21). Second, further *in situ* high-temperature pXRD analyses were carried out, showing that if the  $\beta$ -polymorph forms at high temperatures (Figure S22), it does not retransform into the  $\alpha$ -phase upon cooling (as also reported in previous works).<sup>17,33</sup> Thus, it seems clear that the anhydrous phase studied by <sup>17</sup>O ssNMR was the  $\alpha$ -form.<sup>17</sup>

In the reported crystal structure of  $\alpha$ -COA (*C2/m* space group),<sup>17,33</sup> there are 2 inequivalent carbon and 3 inequivalent oxygen sites, with one of the oxygen atoms placed in a special position. While the high-temperature <sup>13</sup>C ssNMR of anhydrous calcium oxalate shows two resonances (Figure 6a), the <sup>17</sup>O MQMAS spectrum shows 4 resolved resonances (Figure 7b). The raw crystallographic data of the reported structure was thus reanalyzed in detail. It was noticed that the thermal ellipsoids for two of the oxalate atoms (numbered O<sub>2</sub> and C<sub>2</sub> in the previously reported crystal structure)<sup>17</sup> were more pronounced than the others, suggesting unresolved disorder or the presence of a pseudoinversion center instead of a real one. To try to reconcile XRD and NMR results, two possibilities were considered: (i) a different space group for the crystallographic data (with *C2* symmetry, implying notably the symmetry independence of two O<sub>2</sub> sites which are symmetry-equivalent in *C2/m*), and (ii) a small disorder around C<sub>2</sub> and O<sub>2</sub> positions within the *C2/m* space group.

Regarding the first option, attempts to refine the structure in the *C2* space group were unsatisfactory: correlations were too large to get a stable refinement and accordingly nice ellipsoids. Moreover, for this possibility to be valid, equal relative intensities of the four oxygen sites should have been observed in the quantitative 1D <sup>17</sup>O ssNMR, which is not the case in our fits (see Figure S20). Additionally, we performed a periodic DFT optimization of this structure without imposing *C2/m* symmetry constraints (i.e., in space group *P1*), and then analyzed quantitatively the resulting structure with respect to the presence or absence of the symmetry operators of space group *C2/m*. For this, we used the reciprocal space method developed for the detection of symmetry elements in *P1* electron density maps in the context of iterative structure solution methods in crystallography.<sup>78</sup> The results of this symmetry analysis are without any ambiguity: the relaxed *P1* structure has true *C2/m* symmetry. This is in line with the very small (and nearly insignificant) DFT energy drop  $-0.49797$  eV, obtained after the release of the symmetry constraints in *C2/m*. Overall, all of these analyses tend to show that the *C2/*

*m* space group is correct, but that the structure presents a small positional disorder on some of the atomic positions.

In <sup>17</sup>O ssNMR, the signals attesting of this crystallographic disorder are most likely those which have the most similar NMR parameters (in the central part of the spectrum), with a relative intensity  $\sim 0.16$  (sites referred to as O<sub>12</sub>/O<sub>13</sub> in Figures 7, S19, and S20). Assignment of the other two  $\alpha$ -COA oxygen sites observed in <sup>17</sup>O NMR was performed (i) by carefully assessing the structures of the HT-COM and COA, and comparing their relative <sup>17</sup>O chemical shifts, and (ii) using complementary GIPAW-DFT calculations. First, looking at the relationships between the structures, it appears that O<sub>10</sub> and O<sub>11</sub> in HT-COM become O<sub>14</sub> and O<sub>15</sub>, respectively, in  $\alpha$ -COA (Figure S1). Supposing that the relative isotropic chemical shifts of these two sites remain the same upon formation of the anhydrous form, this would lead to O<sub>14</sub> being the site with the highest  $\delta_{\text{iso}}$  value (282.4 ppm), and O<sub>15</sub> the other (242.6 ppm). GIPAW-DFT calculations were carried out, using as a model for  $\alpha$ -COA the previously reported crystal structure (i.e., with no disorder),<sup>33</sup> and relaxing atomic positions (see Table S8). The highest and lowest calculated chemical shifts were found to correspond respectively to O<sub>14</sub> and O<sub>15</sub>, and an intermediate shift was found for the remaining oxygen site. The relative order of calculated  $C_Q$  and  $\eta_Q$  parameters for these resonances was also found to agree with experimental data, thereby confirming the proposed assignment.

Overall, this study on  $\alpha$ -COA further demonstrates the usefulness of <sup>17</sup>O ssNMR for analyzing the crystalline structure of oxalate materials in detail. Notably, for this phase, the <sup>17</sup>O chemical shift range spans over  $\approx 36$  ppm, which enabled to resolve a small <sup>17</sup>O resonance attesting of positional disorder in the material, with a small occupancy. In contrast, the <sup>13</sup>C chemical shift range is much more limited ( $< 2$  ppm), preventing from picking up such subtleties in the structure.

## CONCLUSIONS

We have successfully shown that oxalate anions can be isotopically enriched in oxygen-17 using mechanochemistry, resulting in a good enrichment level. The given enrichment protocol was used to prepare enriched COM biominerals, and further expanded to obtain carbon-13 enriched and even doubly labeled minerals. The prepared samples were then further used to follow by *in situ* ssNMR analyses the phase transitions upon heat treatment, from the LT to the HT forms of COM, and then the anhydrous  $\alpha$ -COA phase. Using high-resolution oxygen-17 ssNMR, it was possible to resolve and assign the <sup>17</sup>O resonances, and gain new insight into the structures of these minerals. Notably, <sup>17</sup>O NMR was clearly shown to be a very sensitive probe of oxalate binding modes, allowing us to shed light on features that had not been seen so far, including a small amount of positional disorder in  $\alpha$ -COA. Given the large number of functional (bio)materials involving oxalate ions, this work expands beyond some of the early <sup>17</sup>O solution NMR studies on oxalate binding in biomolecules,<sup>79,80</sup> and clearly demonstrates the added value of using <sup>17</sup>O labeling in structural analyses using NMR crystallography approaches.

## ASSOCIATED CONTENT

### Supporting Information

The Supporting Information is available free of charge at <https://pubs.acs.org/doi/10.1021/acs.inorgchem.4c00300>.

Complementary IR, pXRD, and MS analyses of the materials; ssNMR acquisition parameters; computational details; fits of  $^{17}\text{O}$  NMR spectra of LT- and HT-COM, and of  $\alpha$ -COA; variable-temperature  $^{13}\text{C}$  NMR spectra; variable-temperature pXRD data; and representations of the structural correspondence between the different phases (PDF)

## AUTHOR INFORMATION

### Corresponding Authors

Ieva Goldberga – ICGM, Univ Montpellier, CNRS, ENSCM, 34293 Montpellier, France; Present Address: LCMCP, UMR 7574, Sorbonne Université, CNRS, 75005 Paris, France; [orcid.org/0000-0003-4284-3527](https://orcid.org/0000-0003-4284-3527); Email: [ieva.goldberga@sorbonne-universite.fr](mailto:ieva.goldberga@sorbonne-universite.fr)

Christel Gervais – LCMCP, UMR 7574, Sorbonne Université, CNRS, 75005 Paris, France; [orcid.org/0000-0001-7450-1738](https://orcid.org/0000-0001-7450-1738); Email: [christel.gervais\\_stary@sorbonne-universite.fr](mailto:christel.gervais_stary@sorbonne-universite.fr)

Danielle Laurencin – ICGM, Univ Montpellier, CNRS, ENSCM, 34293 Montpellier, France; [orcid.org/0000-0002-7445-0528](https://orcid.org/0000-0002-7445-0528); Email: [danielle.laurencin@umontpellier.fr](mailto:danielle.laurencin@umontpellier.fr)

### Authors

Ivan Hung – National High Magnetic Laboratory (NHMFL), Tallahassee, Florida 32310, United States; [orcid.org/0000-0001-8916-739X](https://orcid.org/0000-0001-8916-739X)

Vincent Sarou-Kanian – CNRS, CEMHTI UPR3079, Université d'Orléans, 45071 Orléans, France; [orcid.org/0000-0001-9611-8377](https://orcid.org/0000-0001-9611-8377)

Zhehong Gan – National High Magnetic Laboratory (NHMFL), Tallahassee, Florida 32310, United States; [orcid.org/0000-0002-9855-5113](https://orcid.org/0000-0002-9855-5113)

Jessica Novák Špačková – ICGM, Univ Montpellier, CNRS, ENSCM, 34293 Montpellier, France; Present Address: Synthon, 67801 Blansko, Czech Republic.

Thomas-Xavier Métro – ICGM, Univ Montpellier, CNRS, ENSCM, 34293 Montpellier, France; [orcid.org/0000-0003-2280-3595](https://orcid.org/0000-0003-2280-3595)

César Leroy – ICGM, Univ Montpellier, CNRS, ENSCM, 34293 Montpellier, France; [orcid.org/0000-0002-9013-5552](https://orcid.org/0000-0002-9013-5552)

Dorothee Berthomieu – ICGM, Univ Montpellier, CNRS, ENSCM, 34293 Montpellier, France; [orcid.org/0000-0002-3818-105X](https://orcid.org/0000-0002-3818-105X)

Arie van der Lee – IEM, Univ Montpellier, CNRS, ENSCM, 34095 Montpellier, France; [orcid.org/0000-0002-4567-1831](https://orcid.org/0000-0002-4567-1831)

Christian Bonhomme – LCMCP, UMR 7574, Sorbonne Université, CNRS, 75005 Paris, France; [orcid.org/0000-0003-0802-6961](https://orcid.org/0000-0003-0802-6961)

Complete contact information is available at:

<https://pubs.acs.org/10.1021/acs.inorgchem.4c00300>

### Author Contributions

The project was conducted by I.G., in close interaction with D.L. I.G. carried out the isotopic enrichment experiments, characterizations by IR, MS, and pXRD, as well as the vast majority of ssNMR experiments. I.H. and Z.G. performed the high-resolution experiments at 18.8 and 35.2 T (including variable-temperature studies on the LT to HT phase transition), and I.H. participated in data analysis. V.S.-K.

participated in the high-temperature  $^{17}\text{O}$  NMR experiments recorded at 17.6 T (Orléans) and the study on COA. I.G. and C.G. carried out GIPAW-DFT computations, C.G. performed the MD calculations, and D.B. and D.L. participated in discussions on computational results. J.N.-S. and T.-X.M. participated in discussions on mechanochemistry labeling reactions. C.G., C.L., and C.B. participated in discussions on ssNMR data of calcium oxalates. A.v.d.L. performed the crystallographic study of the COA phase. I.G. and D.L. wrote the initial draft of the manuscript (deposited as a preprint),<sup>81</sup> and all authors contributed to the final preparation of the article.

### Notes

The authors declare no competing financial interest.

## ACKNOWLEDGMENTS

This project has received funding from the European Research Council (ERC) under the European Union's Horizon 2020 research and innovation program (grant agreement no. 772204; 2017 ERC COG, MISOTOP project). DFT calculations were performed using HPC resources from GENCI-IDRIS (grants nos. 097535, 2020-A0090807394, 2021-A0110807394, and 2024-AD010815148). Financial support from the IR INFRANALYTICS FR2054 for conducting part of the NMR research at the CEMHTI facility in Orléans is gratefully acknowledged. A portion of this work was also performed at the National High Magnetic Field Laboratory, which is supported by the National Science Foundation Cooperative Agreements Nos. DMR-1644779 and DMR-2128556 and the State of Florida. The majority of powder X-ray diffraction characterizations were performed with the support of the local Balard Plateforme d'Analyses et de Caractérisation (PAC Balard) and of Dominique Granier and Bernard Fraisse. Margarita Shepelenko and co-workers (Weizmann Institute of Science) are acknowledged for providing a model of the HT-COM structure and discussions. Pierre Florian (CEMHTI, Orléans) is thanked for discussions on the variable-temperature/high-field ssNMR experiments. Guillaume Cazals (IBMM, Montpellier) is acknowledged for his assistance in MS analyses.

## REFERENCES

- (1) Yeoh, J. S.; Armer, C. F.; Lowe, A. Transition Metal Oxalates as Energy Storage Materials. A Review. *Mater. Today Energy* **2018**, *9*, 198–222.
- (2) Huskić, I.; Friščić, T. Geomimetic Approaches in the Design and Synthesis of Metal-Organic Frameworks. *Philos. Trans. R. Soc., A* **2019**, *377* (2149), No. 20180221, DOI: [10.1098/rsta.2018.0221](https://doi.org/10.1098/rsta.2018.0221).
- (3) Thorarinsdottir, A. E.; Harris, T. D. Metal-Organic Framework Magnets. *Chem. Rev.* **2020**, *120* (16), 8716–8789.
- (4) Cui, R.; Li, R.; Li, Z.; Wei, M.; Wang, X.; Li, X. A Tb-MOF Anion, Porous Coordination Framework Constructed with Oxalate Ligand: Crystal Structure, Adsorption Properties, and Luminescence Sensing. *Dyes Pigm.* **2021**, *195*, No. 109669.
- (5) Akhtar, M. N.; Chen, Y.-C.; AlDamen, M. A.; Tong, M.-L. 3D Oxalato-Bridged Lanthanide(III) MOFs with Magnetocaloric, Magnetic and Photoluminescence Properties. *Dalton Trans.* **2017**, *46* (1), 116–124.
- (6) Liu, C.-M.; Zhang, D.-Q.; Zhu, D.-B. Slow Magnetic Relaxation of a Three-Dimensional Metal–Organic Framework Featuring a Unique Dysprosium(III) Oxalate Layer. *RSC Adv.* **2015**, *5* (78), 63186–63192.

- (7) Sanchez, C.; Shea, K. J.; Kitagawa, S.; Schubert, U. Multifunctionality in Hybrid Magnetic Materials Based on Bimetallic Oxalate Complexes. *Chem. Soc. Rev.* **2011**, *40* (2), 453–1152.
- (8) Abraham, F.; Arab-Chapelet, B.; Rivenet, M.; Tamain, C.; Grandjean, S. Actinide Oxalates, Solid State Structures and Applications. *Coord. Chem. Rev.* **2014**, *266–267* (1), 28–68.
- (9) Baran, E. J. Natural Iron Oxalates and Their Analogous Synthetic Counterparts: A Review. *Geochemistry* **2016**, *76* (3), 449–460.
- (10) Echigo, T.; Kimata, M. Crystal Chemistry and Genesis of Organic Minerals: A Review of Oxalate and Polycyclic Aromatic Hydrocarbon Minerals. *Can. Mineral.* **2010**, *48* (6), 1329–1358.
- (11) Dutton, M. V.; Evans, C. S. Oxalate Production by Fungi: Its Role in Pathogenicity and Ecology in the Soil Environment. *Can. J. Microbiol.* **1996**, *42* (9), 881–895.
- (12) Giordani, P.; Modenesi, P.; Tretiach, M. Determinant Factors for the Formation of the Calcium Oxalate Minerals, Weddellite and Whewellite, on the Surface of Foliose Lichens. *Lichenologist* **2003**, *35* (3), 255–270.
- (13) Coe, F. L.; Evan, A.; Worcester, E. Kidney Stone Disease. *J. Clin. Invest.* **2005**, *115* (10), 2598–2608.
- (14) Khan, S. R.; Pearle, M. S.; Robertson, W. G.; Gambaro, G.; Canales, B. K.; Doizi, S.; Traxer, O.; Tiselius, H.-G. Kidney Stones. *Nat. Rev. Dis. Primers* **2016**, *2* (1), 16008.
- (15) Daudon, M.; Dessombz, A.; Frochot, V.; Letavernier, E.; Haymann, J.-P.; Jungers, P.; Bazin, D. Comprehensive Morpho-Constitutional Analysis of Urinary Stones Improves Etiological Diagnosis and Therapeutic Strategy of Nephrolithiasis. *C. R. Chim.* **2016**, *19* (11–12), 1470–1491.
- (16) Van de Perre, E.; Bazin, D.; Estrade, V.; Boudier, E.; Wissing, K. M.; Daudon, M.; Letavernier, E. Randall's Plaque as the Origin of Idiopathic Calcium Oxalate Stone Formation: An Update. *C. R. Chim.* **2022**, *25* (S1), 373–391.
- (17) Izatulina, A. R.; Gurzhiy, V. V.; Krzhizhanovskaya, M. G.; Kuz'mina, M. A.; Leoni, M.; Frank-Kamenetskaya, O. V. Hydrated Calcium Oxalates: Crystal Structures, Thermal Stability, and Phase Evolution. *Cryst. Growth Des.* **2018**, *18* (9), 5465–5478.
- (18) Hochrein, O.; Thomas, A.; Kniep, R. Revealing the Crystal Structure of Anhydrous Calcium Oxalate, Ca[C<sub>2</sub>O<sub>4</sub>], by a Combination of Atomistic Simulation and Rietveld Refinement. *Z. Anorg. Allg. Chem.* **2008**, *634* (11), 1826–1829.
- (19) Gehl, A.; Dietzsch, M.; Mondeshki, M.; Bach, S.; Häger, T.; Panthöfer, M.; Barton, B.; Kolb, U.; Tremel, W. Anhydrous Amorphous Calcium Oxalate Nanoparticles from Ionic Liquids: Stable Crystallization Intermediates in the Formation of Whewellite. *Chem. - Eur. J.* **2015**, *21* (50), 18192–18201.
- (20) Shepelenko, M.; Feldman, Y.; Leiserowitz, L.; Kronik, L. Order and Disorder in Calcium Oxalate Monohydrate: Insights from First-Principles Calculations. *Cryst. Growth Des.* **2020**, *20* (2), 858–865.
- (21) Begun, G. M.; Fletcher, W. H. Vibrational Spectra of Aqueous Oxalate Ion. *Spectrochim. Acta* **1963**, *19* (8), 1343–1349.
- (22) Shippey, T. A. Vibrational Studies of Anhydrous Lithium, Sodium and Potassium Oxalates. *J. Mol. Biol.* **1980**, *67*, 223–233.
- (23) Clark, R. J. H.; Firth, S. Raman, Infrared and Force Field Studies of K<sub>2</sub><sup>12</sup>C<sub>2</sub>O<sub>4</sub>·H<sub>2</sub>O and K<sub>2</sub><sup>13</sup>C<sub>2</sub>O<sub>4</sub>·H<sub>2</sub>O in the Solid State and in Aqueous Solution, and of (NH<sub>4</sub>)<sub>2</sub><sup>12</sup>C<sub>2</sub>O<sub>4</sub>·H<sub>2</sub>O and (NH<sub>4</sub>)<sub>2</sub><sup>13</sup>C<sub>2</sub>O<sub>4</sub>·H<sub>2</sub>O in the Solid State. *Spectrochim. Acta, Part A* **2002**, *58* (8), 1731–1746.
- (24) Frost, R. L.; Weier, M. L. Thermal Treatment of Whewellite—A Thermal Analysis and Raman Spectroscopic Study. *Thermochim. Acta* **2004**, *409* (1), 79–85.
- (25) Echigo, T.; Kimata, M. Single-Crystal X-Ray Diffraction and Spectroscopic Studies on Humboldtine and Lindbergite: Weak Jahn–Teller Effect of Fe<sup>2+</sup> Ion. *Phys. Chem. Miner.* **2008**, *35* (8), 467–475.
- (26) Leroy, C. Oxalates de Calcium et Hydroxyapatite: Des Matériaux Synthétiques et Naturels Étudiés Par Techniques RMN et DNP, PhD Thesis, Université Pierre et Marie Curie: Paris VI, 2016.
- (27) Lee, M.; Schaumburg, K. Coordination-site Exchange and Solid-state <sup>13</sup>C NMR Studies of Bis(Oxalato)Dioxovanadate(V) Ion. *Magn. Reson. Chem.* **1991**, *29* (9), 865–869.
- (28) Zhu, J.; Ye, E.; Tersikh, V.; Wu, G. Solid-State <sup>17</sup>O NMR Spectroscopy of Large Protein–Ligand Complexes. *Angew. Chem., Int. Ed.* **2010**, *49* (45), 8399–8402.
- (29) Kong, X.; Tersikh, V. V.; Khade, R. L.; Yang, L.; Rorick, A.; Zhang, Y.; He, P.; Huang, Y.; Wu, G. Solid-State <sup>17</sup>O NMR Spectroscopy of Paramagnetic Coordination Compounds. *Angew. Chem.* **2015**, *127* (16), 4835–4839.
- (30) Michaelis, V. K.; Keeler, E. G.; Ong, T.-C.; Craigen, K. N.; Penzel, S.; Wren, J. E. C.; Kroeker, S.; Griffin, R. G. Structural Insights into Bound Water in Crystalline Amino Acids: Experimental and Theoretical <sup>17</sup>O NMR. *J. Phys. Chem. B* **2015**, *119* (25), 8024–8036.
- (31) Wong, A.; Pike, K. J.; Jenkins, R.; Clarkson, G. J.; Anupöld, T.; Howes, A. P.; Crout, D. H. G.; Samoson, A.; Dupree, R.; Smith, M. E. Experimental and Theoretical <sup>17</sup>O NMR Study of the Influence of Hydrogen-Bonding on CO and O–H Oxygens in Carboxylic Solids. *J. Phys. Chem. A* **2006**, *110* (5), 1824–1835.
- (32) Wong, A.; Poli, F. *Solid-State <sup>17</sup>O NMR Studies of Biomolecules*, 1st ed.; Elsevier Ltd, 2014; Vol. 83.
- (33) Zhao, W.; Sharma, N.; Jones, F.; Raiteri, P.; Gale, J. D.; Demicheli, R. Anhydrous Calcium Oxalate Polymorphism: A Combined Computational and Synchrotron X-Ray Diffraction Study. *Cryst. Growth Des.* **2016**, *16* (10), 5954–5965.
- (34) Frost, R. L.; Weier, M. L. Thermal Treatment of Weddellite—a Raman and Infrared Emission Spectroscopic Study. *Thermochim. Acta* **2003**, *406* (1–2), 221–232.
- (35) Dollimore, D. The Thermal Decomposition of Oxalates. *Thermochim. Acta* **1987**, *117*, 331–363.
- (36) Goldberga, I.; Patris, N.; Chen, C.-H.; Thomassot, E.; Trébosc, J.; Hung, I.; Gan, Z.; Berthomieu, D.; Métro, T.-X.; Bonhomme, C.; et al. First Direct Insight into the Local Environment and Dynamics of Water Molecules in the Whewellite Mineral Phase: Mechanochemical Isotopic Enrichment and High-Resolution <sup>17</sup>O and <sup>2</sup>H NMR Analyses. *J. Phys. Chem. C* **2022**, *126* (29), 12044–12059.
- (37) Nour, S.; Widdifield, C. M.; Kobera, L.; Burgess, K. M. N.; Errulat, D.; Tersikh, V. V.; Bryce, D. L. Oxygen-17 NMR Spectroscopy of Water Molecules in Solid Hydrates. *Can. J. Chem.* **2016**, *94* (3), 189–197.
- (38) Špačková, J.; Fabra, C.; Cazals, G.; Hubert-Roux, M.; Schmitz-Afonso, I.; Goldberga, I.; Berthomieu, D.; Lebrun, A.; Métro, T.-X.; Laurencin, D. Cost-Efficient and User-Friendly <sup>17</sup>O/ <sup>18</sup>O Labeling Procedures of Fatty Acids Using Mechanochemistry. *Chem. Commun.* **2021**, *57* (55), 6812–6815.
- (39) Métro, T.; Gervais, C.; Martinez, A.; Bonhomme, C.; Laurencin, D. Unleashing the Potential of <sup>17</sup>O NMR Spectroscopy Using Mechanochemistry. *Angew. Chem., Int. Ed.* **2017**, *56* (24), 6803–6807.
- (40) Špačková, J.; Goldberga, I.; Yadav, R.; Cazals, G.; Lebrun, A.; Verdié, P.; Métro, T.; Laurencin, D. Fast and Cost-Efficient <sup>17</sup>O-Isotopic Labeling of Carboxylic Groups in Biomolecules: From Free Amino Acids to Peptide Chains. *Chem. - Eur. J.* **2023**, *29* (10), No. e202203014.
- (41) MassLynx V4.1, 2024. <https://shorturl.at/DMS78>.
- (42) Harris, R. K.; Becker, E. D.; Cabral De Menezes, S. M.; Granger, P.; Hoffman, R. E.; Zilm, K. W. Further Conventions for NMR Shielding and Chemical Shifts (IUPAC Recommendations 2008). *Pure Appl. Chem.* **2008**, *80* (1), 59–84.
- (43) Morcombe, C. R.; Zilm, K. W. Chemical Shift Referencing in MAS Solid State NMR. *J. Magn. Reson.* **2003**, *162* (2), 479–486.
- (44) Comellas, G.; Lopez, J. J.; Nieuwkoop, A. J.; Lemkau, L. R.; Rienstra, C. M. Straightforward, Effective Calibration of SPINAL-64 Decoupling Results in the Enhancement of Sensitivity and Resolution of Biomolecular Solid-State NMR. *J. Magn. Reson.* **2011**, *209* (2), 131–135.
- (45) Fung, B. M.; Khitrin, A. K.; Ermolaev, K. An Improved Broadband Decoupling Sequence for Liquid Crystals and Solids. *J. Magn. Reson.* **2000**, *142*, 97–101.
- (46) Fernandez, C.; Lang, D. P.; Amoureux, J. P.; Pruski, M. Measurement of Heteronuclear Dipolar Interactions between

Quadrupolar and Spin-1/2 Nuclei in Solids by Multiple-Quantum REDOR NMR. *J. Am. Chem. Soc.* **1998**, *120* (11), 2672–2673.

(47) Gan, Z.; Hung, I.; Wang, X.; Paulino, J.; Wu, G.; Litvak, I. M.; Gor'kov, P. L.; Brey, W. W.; Lendi, P.; Schiano, J. L.; et al. NMR Spectroscopy up to 35.2 T Using a Series-Connected Hybrid Magnet. *J. Magn. Reson.* **2017**, *284*, 125–136.

(48) Amoureux, J.-P.; Fernandez, C. Triple, Quintuple and Higher Order Multiple Quantum MAS NMR of Quadrupolar Nuclei. *Solid State Nucl. Magn. Reson.* **1998**, *10* (4), 211–223.

(49) Cadars, S.; Sein, J.; Duma, L.; Lesage, A.; Pham, T. N.; Baltisberger, J. H.; Brown, S. P.; Emsley, L. The Refocused INADEQUATE MAS NMR Experiment in Multiple Spin-Systems: Interpreting Observed Correlation Peaks and Optimising Lineshapes. *J. Magn. Reson.* **2007**, *188* (1), 24–34.

(50) Martineau, C.; Bouchevreau, B.; Taulelle, F.; Trébosc, J.; Lafon, O.; Paul Amoureux, J. High-Resolution through-Space Correlations between Spin-1/2 and Half-Integer Quadrupolar Nuclei Using the MQ-D-R-INEPT NMR Experiment. *Phys. Chem. Chem. Phys.* **2012**, *14* (19), 7112.

(51) Brinkmann, A.; Kentgens, A. P. M. Proton-Selective  $^{17}\text{O}$ -H Distance Measurements in Fast Magic-Angle-Spinning Solid-State NMR Spectroscopy for the Determination of Hydrogen Bond Lengths. *J. Am. Chem. Soc.* **2006**, *128* (46), 14758–14759.

(52) Rakhmatullin, A.; Simko, F.; Véron, E.; Allix, M.; Martineau-Corcoss, C.; Fitch, A.; Fayon, F.; Shakhovoy, R. A.; Okhotnikov, K.; Sarou-Kanian, V.; et al. X-Ray Diffraction, NMR Studies, and DFT Calculations of the Room and High Temperature Structures of Rubidium Cryolite,  $\text{Rb}_3\text{AlF}_6$ . *Inorg. Chem.* **2020**, *59* (9), 6308–6318.

(53) Thurber, K. R.; Tycko, R. Measurement of Sample Temperatures under Magic-Angle Spinning from the Chemical Shift and Spin-Lattice Relaxation Rate of  $^{79}\text{Br}$  in KBr Powder. *J. Magn. Reson.* **2009**, *196* (1), 84–87.

(54) Daudon, M.; Bazin, D.; André, G.; Jungers, P.; Cousson, A.; Chevallier, P.; Véron, E.; Matzen, G. Examination of Whewellite Kidney Stones by Scanning Electron Microscopy and Powder Neutron Diffraction Techniques. *J. Appl. Crystallogr.* **2009**, *42* (1), 109–115.

(55) Kresse, G.; Furthmüller, J. Efficiency of Ab-Initio Total Energy Calculations for Metals and Semiconductors Using a Plane-Wave Basis Set. *Comput. Mater. Sci.* **1996**, *6* (1), 15–50.

(56) Kresse, G.; Hafner, J. Ab Initio Molecular Dynamics for Liquid Metals. *Phys. Rev. B* **1993**, *47* (1), 558–561.

(57) Giannozzi, P.; Baroni, S.; Bonini, N.; Calandra, M.; Car, R.; Cavazzoni, C.; Ceresoli, D.; Chiarotti, G. L.; Cococcioni, M.; Dabo, I.; et al. QUANTUM ESPRESSO: A Modular and Open-Source Software Project for Quantum Simulations of Materials. *J. Phys.: Condens. Matter* **2009**, *21* (39), No. 395502.

(58) Perdew, J. P.; Burke, K.; Ernzerhof, M. Generalized Gradient Approximation Made Simple. *Phys. Rev. Lett.* **1996**, *77* (18), 3865–3868.

(59) Troullier, N.; Martins, J. L. Efficient Pseudopotentials for Plane-Wave Calculations. *Phys. Rev. B* **1991**, *43* (3), 1993–2006.

(60) Bylander, D. M.; Kleinman, L. Efficacious Form for Model Pseudopotentials. *Phys. Rev. Lett.* **1982**, *48* (20), 1425–1428.

(61) Pickard, C. J.; Mauri, F. All-Electron Magnetic Response with Pseudopotentials: NMR Chemical Shifts. *Phys. Rev. B* **2001**, *63* (24), No. 245101.

(62) Kutzelnigg, W.; Fleischer, U.; Schindler, M. The IGLO-Method: Ab-Initio Calculation and Interpretation of NMR Chemical Shifts and Magnetic Susceptibilities. In *Deuterium and Shift Calculation*; Springer: Berlin, Heidelberg, 1991; Vol. 23, pp 165–262.

(63) Profeta, M.; Benoit, M.; Mauri, F.; Pickard, C. J. First-Principles Calculation of the  $^{17}\text{O}$  NMR Parameters in Ca Oxide and Ca Aluminosilicates: The Partially Covalent Nature of the Ca–O Bond, a Challenge for Density Functional Theory. *J. Am. Chem. Soc.* **2004**, *126* (39), 12628–12635.

(64) Wong, A.; Thurgood, G.; Dupree, R.; Smith, M. E. A First-Principles Computational  $^{17}\text{O}$  NMR Investigation of Metal Ion–

Oxygen Interactions in Carboxylate Oxygens of Alkali Oxalates. *Chem. Phys.* **2007**, *337* (1–3), 144–150.

(65) Pyykkö, P. Year-2017 Nuclear Quadrupole Moments. *Mol. Phys.* **2018**, *116* (10), 1328–1338.

(66) Herzfeld, J.; Berger, A. E. Sideband Intensities in NMR Spectra of Samples Spinning at the Magic Angle. *J. Chem. Phys.* **1980**, *73* (12), 6021–6030.

(67) VandeVondele, J.; Krack, M.; Mohamed, F.; Parrinello, M.; Chassaing, T.; Hutter, J. Quickstep: Fast and Accurate Density Functional Calculations Using a Mixed Gaussian and Plane Waves Approach. *Comput. Phys. Commun.* **2005**, *167* (2), 103–128.

(68) Grimme, S.; Antony, J.; Ehrlich, S.; Krieg, H. A Consistent and Accurate Ab Initio Parametrization of Density Functional Dispersion Correction (DFT-D) for the 94 Elements H–Pu. *J. Chem. Phys.* **2010**, *132* (15), No. 154104.

(69) Goedecker, S.; Teter, M.; Hutter, J. Separable Dual-Space Gaussian Pseudopotentials. *Phys. Rev. B* **1996**, *54* (3), 1703–1710.

(70) VandeVondele, J.; Hutter, J. Gaussian Basis Sets for Accurate Calculations on Molecular Systems in Gas and Condensed Phases. *J. Chem. Phys.* **2007**, *127* (11), No. 114105.

(71) van Meerten, S. G. J.; Franssen, W. M. J.; Kentgens, A. P. M. SsNake: A Cross-Platform Open-Source NMR Data Processing and Fitting Application. *J. Magn. Reson.* **2019**, *301*, 56–66.

(72) MATLAB, version 2021b; The Math Works, Inc., 2021. <https://www.mathworks.com/>.

(73) Colas, H.; Bonhomme-Courry, L.; Diogo, C. C.; Tielens, F.; Babonneau, F.; Gervais, C.; Bazin, D.; Laurencin, D.; Smith, M. E.; Hanna, J. V.; et al. Whewellite,  $\text{CaC}_2\text{O}_4 \cdot \text{H}_2\text{O}$ : Structural Study by a Combined NMR, Crystallography and Modelling Approach. *CrystEngComm* **2013**, *15* (43), 8840.

(74) Leroy, C.; Bonhomme-Courry, L.; Gervais, C.; Tielens, F.; Babonneau, F.; Daudon, M.; Bazin, D.; Letavernier, E.; Laurencin, D.; Iuga, D.; et al. A Novel Multinuclear Solid-State NMR Approach for the Characterization of Kidney Stones. *Magn. Reson.* **2021**, *2* (2), 653–671.

(75) Keeler, E. G.; Michaelis, V. K.; Griffin, R. G.  $^{17}\text{O}$  NMR Investigation of Water Structure and Dynamics. *J. Phys. Chem. B* **2016**, *120* (32), 7851–7858.

(76) Keeler, E. G.; Michaelis, V. K.; Wilson, C. B.; Hung, I.; Wang, X.; Gan, Z.; Griffin, R. G. High-Resolution  $^{17}\text{O}$  NMR Spectroscopy of Structural Water. *J. Phys. Chem. B* **2019**, *123* (14), 3061–3067.

(77) Mazurek, A. H.; Szeleszczuk, L.; Pisklak, D. M. A Review on Combination of Ab Initio Molecular Dynamics and NMR Parameters Calculations. *Int. J. Mol. Sci.* **2021**, *22* (9), 4378.

(78) Palatinus, L.; van der Lee, A. Symmetry Determination Following Structure Solution in P1. *J. Appl. Crystallogr.* **2008**, *41* (6), 975–984.

(79) Zhu, J.; Wu, G. Quadrupole Central Transition  $^{17}\text{O}$  NMR Spectroscopy of Biological Macromolecules in Aqueous Solution. *J. Am. Chem. Soc.* **2011**, *133* (4), 920–932.

(80) Zhu, J.; Kwan, I. C. M.; Wu, G. Quadrupole-Central-Transition  $^{17}\text{O}$  NMR Spectroscopy of Protein-Ligand Complexes in Solution. *J. Am. Chem. Soc.* **2009**, *131* (40), 14206–14207.

(81) Goldberga, I.; Hung, I.; Sarou-Kanian, V.; Gervais, C.; Gan, Z.; Novák-Špačková, J.; Métro, T.-X.; Leroy, C.; Berthomieu, D.; van der Lee, A.; Bonhomme, C.; Laurencin, D. High-Resolution  $^{17}\text{O}$  Solid-State NMR as a Unique Probe for Investigating Oxalate Binding Modes in Materials: The Case Study of Calcium Oxalate Biominerals; ChemRxiv, 2024.